INVESTIGATION OF SIZE SPECIFIC Fe_2O_3 NANOPARTICLES: TOWARDS SINGLE NANOPARTICLE RESOLVED SPECTRO-PTYCHOGRAPHY

A Thesis Submitted to the
College of Graduate and Postdoctoral Studies
In Partial Fulfillment of the Requirements
For the Degree of Master of Science
In the Department of Chemistry
University of Saskatchewan
Saskatoon

By

THEOPHILUS OLUMORIN, BSc (HON)

PERMISSION TO USE

In presenting this thesis in partial fulfillment of the requirements for a postgraduate degree from the University of Saskatchewan, I agree that the Libraries of this University may make it freely available for inspection. I further agree that permission for copying of this thesis in any manner, in whole or in part, for scholarly purposes may be granted by my supervisor Dr. Stephen Urquhart, or in his absence, by the current Head of the Department of Chemistry or the Dean of the College of Graduate and Postdoctoral Studies. It is understood that any copying or publication or use of this thesis or parts thereof for financial gain shall not be allowed without my written permission. It is also understood that due recognition shall be given to me and to the University of Saskatchewan in any scholarly use that may be made of any material in my thesis. Request for the permission to copy or to make other use of the material in this thesis in whole or in part should be addressed to:

Dean

College of Graduate and Postdoctoral Studies

University of Saskatchewan

116 Thorvaldson Building, 110 Science Place

Saskatoon, Saskatchewan S7N 5C9

Canada.

OR

Head

Department of Chemistry

University of Saskatchewan

170 Thorvaldson Building, 110 Science Place

Saskatoon, Saskatchewan S7N 5C9

Canada.

DISCLAIMER

The names of certain commercial products were exclusively used to meet the thesis and/or exhibition requirements for the degree of Master of Science at the University of Saskatchewan. Reference in this dissertation to any specific commercial products, process, or service by trade name, trademark, manufacturer, or otherwise, does not constitute or imply its endorsement, recommendation, or favoring by the University of Saskatchewan. The views and opinions of the author expressed herein do not necessarily state or reflect those of the University of Saskatchewan and shall not be used for advertising or product endorsement purposes.

ABSTRACT

Ptychography is a scanning coherent diffraction imaging technique, where an unlimited field of view can be probed with a high spatial resolution. This technique relies on the increased coherent flux from third-generation synchrotron sources to measure the absorption and phase of a sample. Since ptychography is not limited by the properties of a focusing lens as is the case in many imaging techniques, it has the potential to reach the atomic regime. In practice, there are barriers to overcome to reach the analytical limit of ptychography. For example, the data process required to reconstruct diffraction images to real space images can be computationally intensive.

In this thesis, experiments were designed to understand these barriers and propose solutions to work towards achieving single nanoparticle resolved spectro-ptychography. Iron oxide nanoparticles, specifically α-Fe_2O_3 were used because they are well characterized, have a sharp core edge, and the ptychography imaging detector is sensitive to X-rays at this energy. Therefore, iron oxide nanoparticles were ideal to study with spectro-ptychography and to identify challenges within the acquisition, dataflow, and analysis. Here, we first compare conventional Scanning Transmission X-ray Microscopy (STXM) imaging with ptychographic imaging and then use ptychography images to obtain spectra. Both STXM and ptychography are spectro-microscopy techniques based on Near Edge X-ray Absorption Fine Structure (NEXAFS) spectroscopy, which provides elemental and chemical sensitivity. In this thesis, NEXAFS spectro-ptychography was used to obtain the Fe $L_{2,3}$ NEXAFS absorption and phase spectra.

The phase signal is theoretically related to the absorption spectrum through Kramers-Kronig integral. This thesis will use the Fe $L_{2,3}$ NEXAFS absorption spectra of iron oxide nanoparticles to discuss the relationship between absorption and phase. The measured phase spectra obtained from ptychography are compared with the calculated phase spectra. Lastly, this thesis will summarize some of the critical experimental factors that will play a role in improving spectro-ptychography to realize the broad goal of obtaining well-resolved single nanoparticle spectra.

ACKNOWLEDGMENTS

I would first like to thank my supervisor, Dr. Stephen Urquhart, for his guidance and expertise during my graduate studies. Thank you for your patience, constructive feedback, and support. This is duly appreciated. I would also like to thank the beamline scientist and staff at Canadian Light Source for their help with experiments. Specifically, Dr. Jian Wang, Dr. Charan Kuppili, Dr. Jay Dynes, and Dr. Yingshen Lu. Thank you for enabling a user-friendly environment and for your insights into this work. Special thanks to Larhonda Sobchishin and Eiko Kawamura at the Western College of Veterinary Medicine, WCVM Imaging center for their help with TEM imaging relevant to this work.

I would also like to thank my past and present group members for all their support and encouragement. Thank you, Sam Netzke, Ruhisha Anand, Amara Zuhaib, Sahan Pererra and Radhika Varshney. Lastly, I would like to thank my advisory committee members Dr. Rob Scott and Dr. Lee Wilson for their insights and thought-provoking questions. A big thank you to everyone who has helped me at the Department of Chemistry, University of Saskatchewan. I appreciate learning from everyone.

This research was funded by an NSERC grant awarded to Dr. Stephen Urquhart. STXM-Ptychography measurements were performed at the Canadian Light Source, beamline 101D1. The Canadian Light Source is a national research facility at the University of Saskatchewan supported by the Canada Foundation for Innovation CFI, NSERC, University of Saskatchewan, Canadian Institute of Health Research CIHR, and Government of Saskatchewan.

SOFTWARE USED IN THIS THESIS

- aXis2000 (Analysis of X-ray images and spectra). This software was developed and is maintained by Dr. Adam Hitchcock. It contains code contributions from by Drs. Chris Jacobsen, Carl Zimba, and many others. Available for non-commercial use at http://unicorn.mcmaster.ca/axis/aXis2000-IDLVM.html
- IDL (Interactive Data Language) version 8.1, 8.3, and 8.7 by Harris Geospatial https://www.harrisgeospatial.com/Software-Technology/IDL
- KK_GUI program for Kramers-Kronig calculations developed by Dr. Chris Jacobsen *et al.*[8] on IDL
- Spyder (Python 3.6)
- CUDA-based software package for Ptychography reconstruction called SHARP. Used at Advanced Light Source and US Department of Energy Light Sources. http://camera.lbl.gov/sharp
- ImageJ: Java image processing program

TABLE OF CONTENTS

LIST OF FIGURES

LIST OF TABLES

LIST OF ABBREVIATIONS

CDI – Coherent Diffractive Imaging

CLS – Canadian Light Source

CUDA – Compute Unified Device Architecture

DLS – Dynamic Light Scattering

EPU – Elliptically Polarized Undulator

EXAFS – Extended X-ray Absorption Fine Structure

FEL – Free Electron Lasers

GPU – Graphics Processing Unit

GUI – Graphical User Interface

IP – Ionization Potential

KK – Kramers-Kronig

NEXAFS – Near Edge X-ray Absorption Fine Structure

OD – Optical Density

OSA – Order Sorting Aperture

PIE – Ptychographical Iterative Engine

ROI – Region of Interest

SHARP – Scalable Heterogeneous Adaptive Real-time Ptychography

SiN_x – Silicon Nitride

SM – Spectro Microscopy

SPEM – Scanning Photoelectron Microscopy

STXM – Scanning Transmission X-ray Microscopy

TEM – Transmission Electron Microscopy

TXM – Transmission X-ray Microscopy

WCVM – Western College of Veterinary Medicine

XAS – X-ray Absorption Microscopy

ZP – Zone plate

CHAPTER 1 INTRODUCTION

1.1 Overview

Spectro-microscopy is a technique that combines spectroscopy with imaging information. This can be used to provide information about materials including their structural and chemical composition. There are many types of spectro-microscopy techniques since most forms of imaging and spectroscopy can be combined with some ingenuity.[1] For simplicity, this work will focus on soft X-ray spectro-microscopy (50-3000 eV) with soft X-rays from a synchrotron source. Examples of soft X-ray spectro-microscopy techniques include scanning transmission X-ray microscopy STXM and scanning photoelectron microscopy SPEM.[1-3] These spectro-microscopy techniques can be used to map out the localized distribution of chemical components. More importantly, the ability to utilize near-edge X-ray absorption fine structure, (NEXAFS) as a contrast mechanism makes spectro-microscopy a useful characterization tool.[1] This chapter will introduce fundamental concepts relevant to this thesis and highlight the objective of this work.

1.2 X-ray interactions with matter

A beam of X-ray passing through a sample is absorbed to an extent depending on the thickness of the sample, its density, and the composition of the sample. Equation 1.1 shows the differential equation that describes the attenuation of light as it passes through a sample.

$$-dI = I(z)\mu_l dz \qquad 1.1$$

Where $I(z)$ is the intensity of the beam, dI is the attenuation, dz is the thickness of the sample, and μ_l is the linear absorption coefficient of components in the sample.[4]

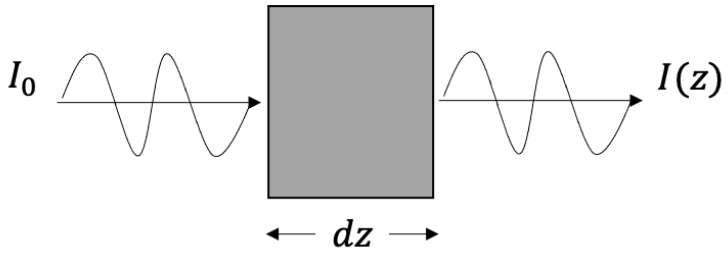

Figure 1.1. A schematic of a photo-absorption process where I_0 is the incident photon on a sample with a thickness of dz and a decrease in intensity $I(z)$ as a function of the sample thickness.

The integrated form of equation 1.1 can be written as $I(z) = I_0 \cdot e^{-\mu_l z}$. On a microscopic scale, this can be further explained in terms of the atomic number density ρ_a and the absorption cross-section σ_a such that:[4]

$$I(z) = I_0 \cdot e^{-\rho_a \sigma_a z} \qquad 1.2$$

The X-ray absorption cross-section of an atom or molecule is typically defined as the number of electrons excited per unit time divided by the number of incident photons per unit time per unit area.[5] Therefore, this cross-section can be calculated for single isolated atoms, and it includes the contributions of various atomic subshells.[6] Figure 1.2 shows an example of the atomic absorption cross-section for carbon as a function of photon energy. In this example, there are contributions from other non-absorption-related processes, such as elastic (coherent) and Compton scattering (inelastic or incoherent). However, the probability of absorption is much higher than scattering within the soft X-ray energy range.[2] More so, Compton scattering is negligible for soft X-rays, therefore it is only absorption and elastic scattering that needs to be considered.[2]

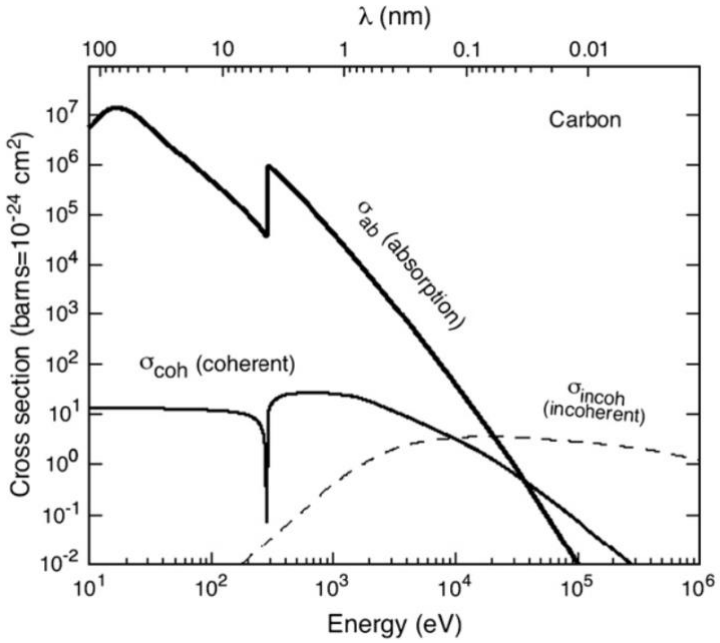

Figure 1.2. Atomic photo-absorption cross-section of Carbon. The total cross-section is the sum of the absorption cross-section and elastic scattering. Inelastic scattering is negligible for soft X-rays. Figure reprinted from Ade, H., *et al.*[2], with permission.

1.2.1 Atomic scattering factors

Both atomic interactions mentioned in the previous section (absorption and elastic scattering) can be expressed quantitatively in terms of the complex atomic scattering factors *f*. The atomic form factor describes the scattering of the charge density and anomalous scattering due to the excitation of electrons. In the small-angle limit or forward scattering direction, *f* is an angle independent scattering factor[2] and is denoted as

$$f = f_1 + \mathrm{i}f_2 \qquad 1.3$$

where f_1 and f_2 are the phase advance and intensity attenuation respectively.

1.2.2 Complex index of refraction

X-ray interaction with matter can also be described with the complex index of refraction $n(r, E)$, as a function of a vector *r* and incident photon energy *E*.[2,7] The refractive index of X-rays in a material n, is complex and less than unity, as shown below

$$n(r, E) = 1 - \delta(r, E) + i\beta(r, E) \qquad 1.4$$

Where δ describes the phase-shifting and dispersion properties of condensed matter and β is the absorption index that describes absorption properties.[2] Both energy-dependent terms δ and β can be expressed as the real and imaginary part of the atomic scattering factors f_1 and f_2 such that

$$n(r, E) = 1 - \delta(r, E) + i\beta(r, E) = 1 - K(f_1 + if_2) \qquad 1.5$$

where $K = (n_a r_e \lambda^2 / 2\pi)$, n_a is the number of atoms of type *a* per unit volume, r_e is the classical electron radius and λ is the wavelength.[8] A later section of this chapter will show that the phase shift effect, which is related to elastic scattering, and the absorptive effects related to the absorption cross-section, complement each other.

1.3 X-ray photo-absorption and photoemission

When X-rays are absorbed, this can cause the excitation of core electrons to bound states or the photoemission of core electrons to the continuum, thereby leaving a molecule in an ionized state.[5] This is shown in equations 1.6 and 1.7.

Photo-absorption: $$\mathrm{M} + \mathrm{hv} \longrightarrow \mathrm{M}^{*} \qquad 1.6$$

Photoemission: $$\mathrm{M} + \mathrm{hv} \longrightarrow \mathrm{M}^{+} + \mathrm{e}^{-} \qquad 1.7$$

During photo-absorption, a core hole is formed and a shortlived excited state M^*, is created. In the case of photoemission, an electron is ejected from the atom to form a core excited cation, M^+. There are two distinct core hole decay processes: fluorescent X-ray emission and Auger electron emission.[4] For fluorescent X-ray emission, the core hole is filled by an electron in the outer shell, and the simultaneously emitted radiation is known as fluorescence.[4] In Auger electron emission, the atom adjusts to the core vacancy through a non-radiative process, in which the core hole is filled by an electron from an outer shell, and energy is conserved by the emission of another secondary electron.[4,6] As fluorescent and Auger spectroscopy are not related to this study, these concepts will not be further discussed here.

1.4 NEXAFS spectroscopy

NEXAFS (also referred to as X-ray absorption near edge structure or XANES) spectroscopy measures the photo-absorption cross-section for the excitation or photoionization of core electrons.[9] When the photon energy is just sufficient to ionize a core electron, there is an "edge jump" that occurs at energy specific to the absorbing element. This threshold energy is also referred to as the ionization energy (IE), ionization potential (IP) or binding energy (BE).[2,5] At or above the IE, core electrons can be excited to the continuum of states. In the case of photo-absorption discussed above, bound state transitions involve excitation to final states below the IE.[5] Figure 1.3 illustrates the principle of NEXAFS spectroscopy.

1.4.1 X-ray absorption spectrum

X-ray absorption spectrum can be divided into two parts: the near edge features (NEXAFS) and extended X-ray absorption fine structure (EXAFS), which appear > 50 eV. EXAFS spectroscopy will not be discussed here.

In X-ray notation, the absorption edge can be classified as K-edge, which correspond to the excitation of a 1s electron, L-edge (L_1, L_2, and L_3), which correspond to the excitation of a 2s, $2p_{1/2}$, and $2p_{3/2}$ electron respectively, and so on, while $L_{2,3}$ edge refers to the spin-orbit split 2p shells ($2p_{1/2}$ and $2p_{3/2}$ edges). The 2p edge is split by core hole spin-orbit splitting, which is a result of the interaction between a core hole orbital angular momentum $l = 1$, and the spin angular momentum, $m_s = \pm ½$.[10] A third symbol J can be used to indicate the total angular momentum of the core hole, where $J = l \pm s$.[10] If the orbital angular momentum is 1, the total angular momentum can be either 1/2 or 3/2, thus resulting in two peaks. The following sections

will highlight the near edge features or resonance-like structures for K shell excitation spectra and atomic multiplet effects in L shell excitation spectra.

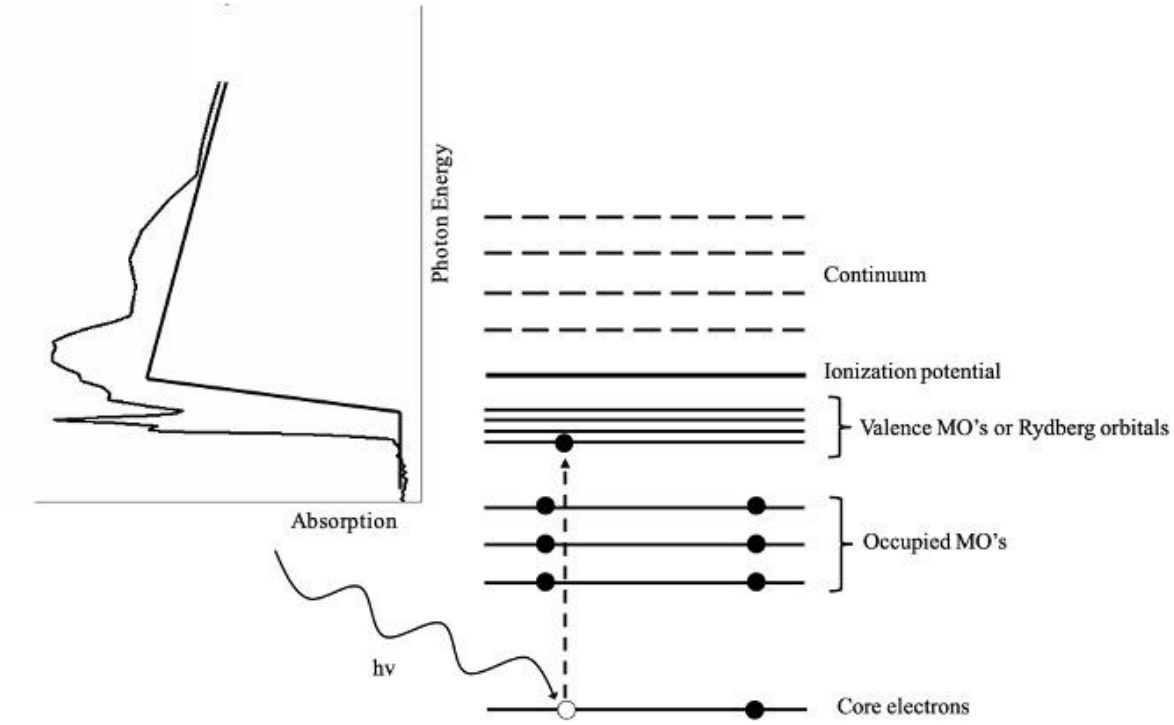

Figure 1.3. Schematic illustrating NEXAFS spectroscopy. Near Edge resonances in the K shell spectra arise from electronic transitions from the ground state to a valence or Rydberg state.

1.5 Characteristic features in K shell spectra

1.5.1 Core to π^* transition

Core to π^* transitions occur in molecules with π bonding. This class of transition has been studied extensively in conjugated polymers[2,9] It is usually the lowest energy structure in low Z molecules and lies below the ionization potential.[5]

1.5.2 Core to Rydberg and mixed-valence resonances

Rydberg orbitals are atomic-like features that lie below the vacuum level (Figure 1.3). In core to Rydberg transitions, the nucleus and all unexcited electrons appear to the excited electron as a single entity with a +1 charge, similar to a hydrogenic nucleus.[11] The energy of Rydberg states follow the Rydberg formula where the Term Value (TV) is

$$TV = IP - E_n = R/(n - \delta_l)^2 \qquad 1.8$$

R is the Rydberg energy, and δ_l is the quantum defect associated with core holes of different symmetry (e.g., $l = 0$ is an s orbital, etc.).

Pure Rydberg states or a mixing of both Rydberg and valence states can exist. The intensity of the Rydberg resonance is generally weak but becomes stronger when mixed with valence orbitals of similar energy and symmetry.[5] Details on Rydberg valence mixing will not be discussed here, as they are not relevant to the species examined in this thesis.

1.5.3 Core to σ^* resonances

Core to σ^* resonances are usually observed above the ionization potential. These transitions are characterized by a broad peak that corresponds to the shorter lifetime of the excited state. The higher the σ^* orbital lie in the continuum, the broader the shape of the resonance and vice versa.[5]

1.6 Multiplet transitions

The above descriptions (π, σ resonances, etc.) refer to electronic transitions in the NEXAFS spectra of organic molecules. In contrast, NEXAFS spectra of 3d transition metals are characterized by 2p to 3d transitions with multiplet splitting, described by atomic multiplet theory. In transition metal oxides, the one-electron excitation description is not applicable for metal $L_{2,3}$ edges. This is because there is a strong overlap between the core wave function and the valence wave function.[12] In the final state, the core orbitals are partly filled as in $2p^5$, which can interact with the partly filled 3d band. For example, in Fe_2O_3, $2p^5$ interacts with the $3d^6$ configuration. It is this strong overlap that creates a set of 2p3d final states and is referred to as an atomic multiplet effect.[12] This intra-atomic effect can be perturbed by the interactions with surrounding atoms, which gives considerable chemical sensitivity.

1.6.1 Crystal field splitting

The effect of the crystal field is based on electrostatic interaction between a metal ion and its ligands.[13] Ligands can be modeled as a negative point charge that repel electrons in the d orbitals of the metal ion. Although there are some drawbacks to this model as it ignores covalent interactions, it is still useful in interpreting the electronic structure and spectroscopy of the metal ion.

In crystal field theory, the five 3d orbitals lose their degeneracy and become split in energy into two distinct representations of t_{2g} and e_g symmetry, for example, when in an octahedral environment.[14] Figure 1.4 shows the energy change of the d orbitals from an ion with no ligands (no point charge source) to a spherical ligand field and lastly to an octahedral ligand field. Crystal field splitting is compounded with multiplet effects to make a rich NEXAFS spectrum.

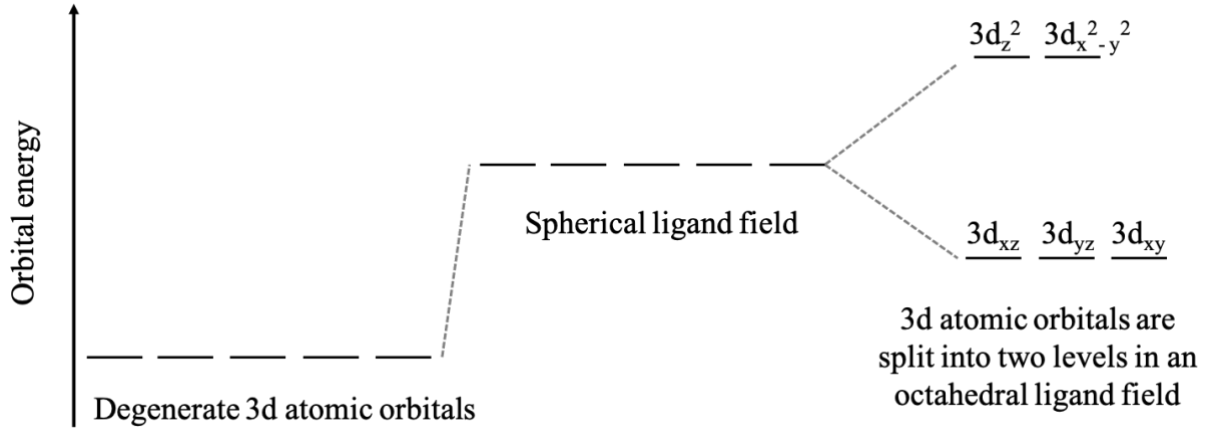

Figure 1.4. The change in energies of electrons occupying the d orbitals of a metal ion. From left to right: Degeneracy of the d orbitals when ligands are at an infinite distance away, spherical ligand field, and octahedral ligand field.

1.7 Dipole selection rules

The transition between initial and final states can be described in terms of the dipole selection rule. The transition dipole moment $\langle\mu\rangle$ is defined with the integral

$$\langle\mu\rangle = \int_0^\infty \psi_{final}^* \, \hat{\mu} \, \psi_{initial} \, dx \qquad 1.9$$

where $\psi_{initial}$ and ψ_{final} are the wavefunctions of the initial and final states, and $\hat{\mu}$ is the dipole operator. A transition is allowed when the dipole moment associated with the transition from one state to another state is non-zero, $\langle\mu\rangle \neq 0$.

An example of the dipole selection rule is the Laporte selection rule of atomic orbitals, where a transition is allowed when $\Delta l = \pm 1$ and the spin is conserved $\Delta s = 0$. The Laporte selection rule is not effective in describing non-centrosymmetric molecules. However, lower symmetry systems (such as iron oxide) follow an atomic propensity rule, where $s \rightarrow p$, $p \rightarrow s$, and $p \rightarrow d$ transitions are found to be strong.

1.8 Why is NEXAFS important in this study?

NEXAFS is known to be sensitive to functional group identity, oxidation states, and the coordination environment of various elements.[5,15] The peak positions and spectral line shape in a NEXAFS spectrum can be directly correlated with the nature of the unoccupied electronic structure.[16] Therefore, NEXAFS can provide information on the electronic structure of each element present in a sample.[10] In this study, the NEXAFS contrast mechanism is used to explore the L edge (2p to 3d transitions) of a transition metal oxide nanomaterial.

1.8.1 Quantitative analysis in NEXAFS

NEXAFS can be used for quantitative analysis. This is because the transmission of photons can be converted to an optical density (OD), following Beer-Lambert law

$$OD = -ln\frac{I}{I_0} = \mu_l \cdot \mathrm{z} = \mu \cdot \rho \cdot z \qquad 1.10$$

where μ is the mass absorption coefficient. The OD is dependent on the property of the sample and is a function of the atomic absorption cross-section (equation 1.2). In the absorption cross section, the size of the edge jump is related to the number of absorbing atoms.[5] Therefore, NEXAFS spectra can be used for quantitative purposes when normalized to the incident photon flux.

1.9 NEXAFS spectroscopy of iron oxide nanoparticles

1.9.1 Properties and structure of iron oxide nanoparticles

Iron-based compounds are interesting because they provide the basis for the design and manufacture of technologically advanced systems.[16] Iron oxides Fe_2O_3 and Fe_3O_4 in particular, exhibit unique optical, electronic, and magnetic properties useful in various applications.[17,18] For example, iron-based nanomaterials are highly favored as catalysts, useful in spintronics, and as information storage devices.[16,19]

Various forms of iron-based materials exist, and they differ in their structure. Common examples are α-Fe_2O_3, γ-Fe_2O_3, and Fe_3O_4. α-Fe_2O_3 nanoparticles, also known as hematite, possess a rhombohedral symmetry (space group R-3c) and corundum structure, where oxygen atoms are arranged in a hexagonal closed packing with Fe^{3+} ions in octahedral sites.[16,20] The

difference in the physical structure of iron-based nanoparticles can be interpreted by their electronic structure.

1.9.2 L edge features in iron oxides

Studies have shown that the NEXAFS spectrum at the Fe 2p edge is characterized by two absorption bands. This is a result of spin-orbit splitting.[16,18] Figure 1.5 shows a narrow band between 705 eV and 715 eV at the L_3 edge (3/2), and a much broad band between 720 eV and 725 eV at the L_2 (1/2) edge. The multiplet effects resulting in individual peaks within each band are more visible at the L_3 edge than at the L_2 edge. This is shown in Figure 1.5 for different types of iron oxide materials.

In an isolated Fe atom ($3d^6\ 4s^2$ configuration), the ground state of the 3d shell is split into 5 J substates by 3d spin-orbit coupling.[14] For a $3d^6$ to $2p^5\ 3d^7$ transition, the 2p3d multiplet interaction for each J state results in many atomic states.[14] It is the combination of these final states that give the fine structure in the spectra.

In 2p X-ray absorption of ionic solids, the crystal field theory acts on the atomic multiplet states.[14] In other words, the fine structure is a combination of final states due to atomic multiplets and the surrounding atoms. However, iron oxides are covalent and cannot be effectively described with crystal field theory. De Groot *et al.*[14] uses charge transfer multiplet theory calculations to describe the L edge features in iron oxides. The charge transfer effects are based on energy differences between different occupations of the 3d states due to the core hole potential.[12] In this work, we will refer to the multiplets in terms of their crystal field splitting. According to crystal field theory, the L_3 edge peak is split into t_{2g} and e_g respectively for an octahedral surrounding. This crystal field splitting is shown in the literature NEXAFS spectra of various iron oxide compounds (Figure 1.5).

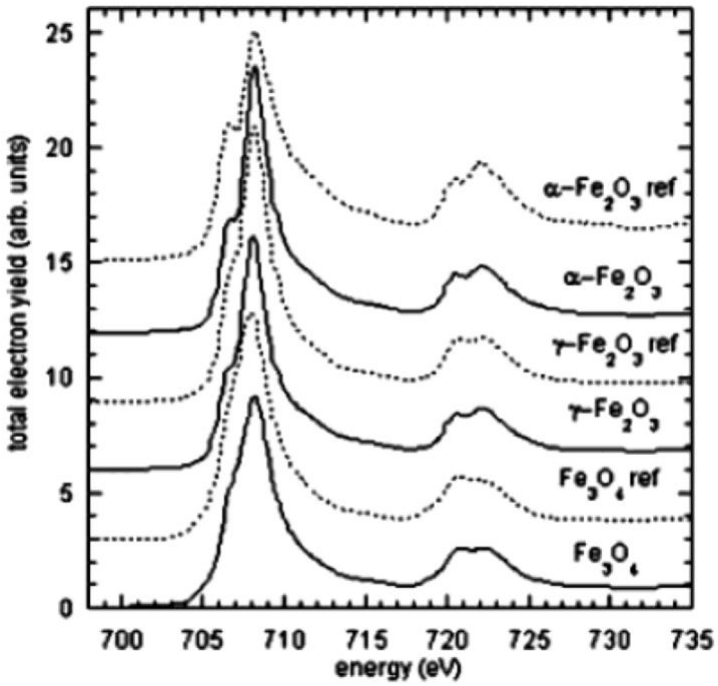

Figure 1.5. Iron 2p NEXAFS spectra of Hematite α-Fe_2O_3, Maghemite γ-Fe_2O_3, and Magnetite Fe_3O_4 nanoparticle assemblies in total electron yield mode. Figure reprinted from Sun, S., *et al.*[18], with permission.

1.10 NEXAFS microscopy

As indicated in previous sections, NEXAFS spectroscopy can be useful in characterizing the chemical composition of materials. In NEXAFS microscopy, imaging can be performed at specific energy or spectra can be obtained by imaging a small spot. In general, NEXAFS microscopy is not as sensitive as other spectroscopic techniques (IR, NMR, etc.) in identifying functional groups and specific moieties. However, its power is mostly based on its ability to exceed the spatial resolution of these other spectroscopic techniques.[9] The following section will discuss the principle of X-ray microscopy with emphasis on the technique related to this work, which is STXM. §1.10.3 will then highlight what spectro-microscopy is and how it fits within the context of this study.

1.10.1 Scanning transmission X-ray microscope (STXM)

STXM is a zone plate-based transmission microscope. Figure 1.6 shows a schematic of STXM on a synchrotron source with an overview of STXM optics. Monochromatic X-rays are focused by the zone plate and the first-order diffraction focus is selected with the order sorting

aperture (OSA), which illuminates the sample before transmission is measured by the STXM detector. An image is then generated from the transmitted photons by raster scanning the sample through the focus spot.

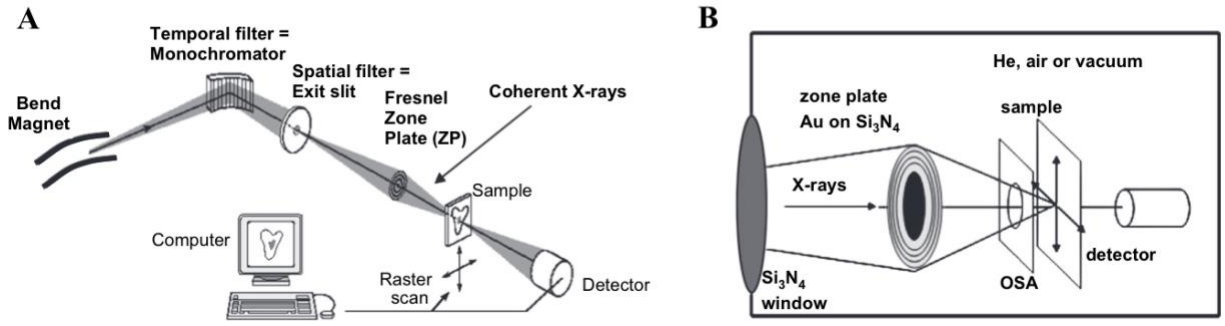

Figure 1.6. A. Schematic of Scanning Transmission X-ray Microscope (STXM) B. STXM optics showing the zone plate, OSA, sample, and detector. Figure reprinted from Ade, H., and Hitchcock, A.[2], with permission.

1.10.2 Spatial resolution in real space imaging

Microscopic techniques that use a lens as the focusing optic are referred to as real-space imaging. STXM is considered a real space imaging technique because of the use of a zone plate as the focusing optic (Figure 1.6 B). The spatial resolution of a STXM is determined by the width of the outermost zone of the zone plate. In other words, the spatial resolution depends on the quality of the zone plate.[2] The Rayleigh resolution of a 'perfect' zone plate is 1.22 times the outermost zone width ($1.22 \times \Delta r_n$).[2] Various studies suggest a typical spatial resolution at about 30 nm for STXM images.[1,2,21] Hitchcock *et al*. notes this to be the case in their study of individual cells in magnetotactic bacteria, with the use of a 25 nm outer zone plate.[22] §1.11 will introduce a relatively new imaging technique called ptychography that has the potential for higher resolution imaging than conventional STXM imaging.

1.10.3 Spectro-microscopy

Spectro-microscopy is the combination of spectroscopy and microscopy. In general, there are two forms to this technique: spectra can be generated at small sample domains, or microscopic images are acquired using electronic transitions to create an image contrast.[11] In the case of the latter, the microscopic images are measured at different energies and are referred to as a 'stack' or image sequence.[2,23] There is a change in image contrast when components of a sample strongly absorb photons at the absorption edge energy. Figure 1.7 illustrates this principle

with the pre-edge image and a series of high contrast images corresponding to strong X-ray absorption.

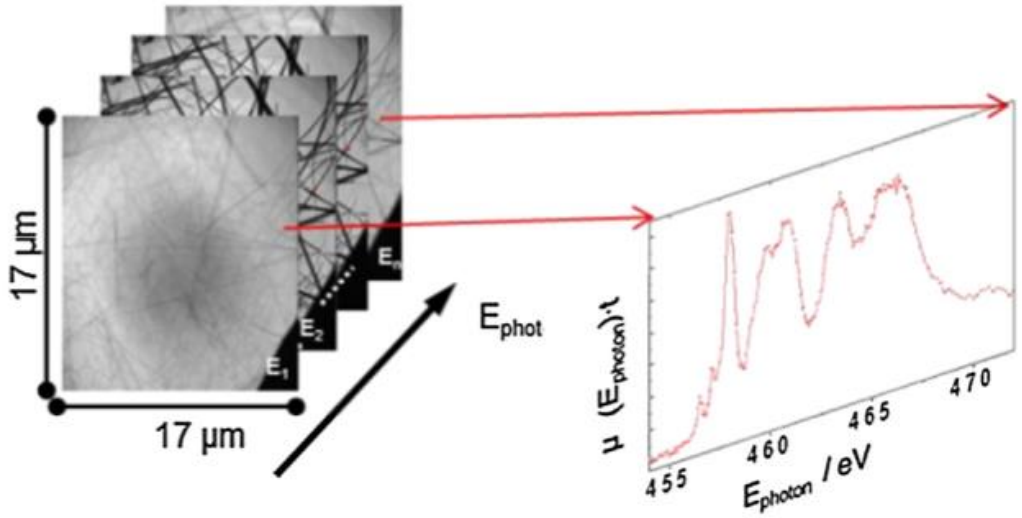

Figure 1.7. Schematic of a TXM based spectro-microscopy data from multi-energy image sequences to spectra. Figure adapted from Guttmann *et al.* licensed under CC BY 3.0.[24]

The image stack allows the chemical mapping of components in a sample, and the ability to distinguish between elements and between different chemical forms of the same element. Therefore, spectro-microscopy with NEXAFS based contrast mechanism can be used to probe specific and small regions or domains in a sample (micro-spectroscopy). This is unlike conventional NEXAFS with a single spot (typically 5-10 micron up to mm in size), where there is an "averaging effect" that may lead to a loss of information when measuring across a sample domain.[5] This study will show the results of a NEXAFS spectro-microscopy technique using iron(III) oxide nanoparticles.

1.11 Ptychography

Ptychography is a coherent diffraction imaging (CDI) technique commonly referred to as a 'lensless' technique. Ptychography involves raster scanning to record a series of diffraction pattern from overlapping spots.[25] The diffraction patterns are then used to make a real space image, through a reconstruction algorithm. Ptychography is 'lensless' because the setup does not require a focusing optic, therefore the sample can either be in focus or out of focus. This means that ptychography eliminates spherical aberrations, low numerical aperture, and diffraction limitations associated with other imaging techniques.[25] Hence, it is capable of measuring higher

resolution images. Figure 1.8A shows a ptychography setup which includes a pinhole, the sample, and a far-field diffraction pattern captured by the ptychography detector. The sample is scanned in the x-y plane while ensuring that there is an overlap between spots (Figure 1.8B). This overlap or so-called 'oversampling process' ensures a high redundancy of information [26] required for the iterative (algorithmic) process used to solve for the sample image. An iterative process reconstructs the diffraction patterns by solving a 'phase problem', a term that is common in the field of X-ray crystallography. In ptychography, the solution of the phase problem can be extended to non-crystalline or non-periodic samples.[27]

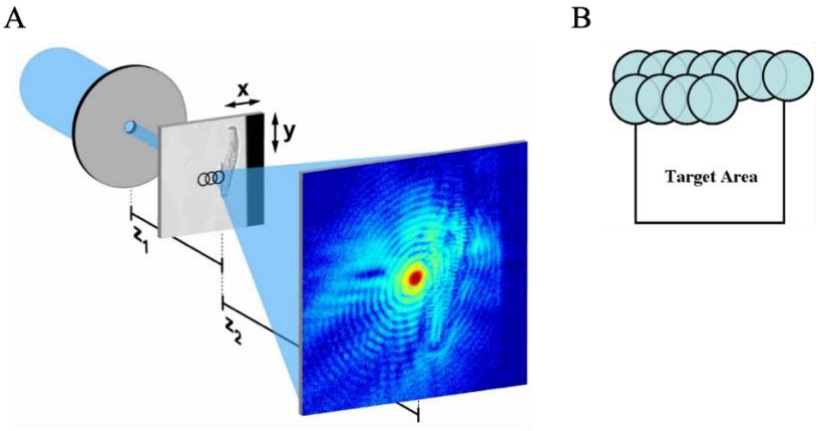

Figure 1.8. A. Schematic of scanning coherent diffraction imaging technique (Ptychography) B. Oversampling of the region of interest or target area is performed in ptychography. Figure adapted from Giewekemeyer, K., *et al*. licensed under CC BY 4.0.[26]

1.11.1 The phase retrieval problem in ptychography

The concept of ptychography was first published by Walter Hoppe in 1969 [28,29] as a solution to the phase problem – where the phase relationship between parts of a wave is lost during experiments leaving only information about the magnitude/ intensity of the wave.[28] The general idea here is to reconstruct the entire wavefield scattered from an object. Although, the advancements we have today were lacking then, Hoppe and Strube [29] were able to demonstrate this idea using visible light optics.[28] This laid the groundwork for future experiments in developing ptychography alongside the improvements made with other imaging techniques.

The far-field diffraction pattern shown in Figure 1.8 describes the multiplicative transmission function of the object $T(r, E)$ and probe function $P(r, E)$ (also referred to as the illumination function falling on the object).[28,30]

$$\psi_{(r)}^{j} = T(r,E) \cdot P(r,E) \quad 1.11$$

Where r is a real space two-dimensional vector, and E is the incident X-ray energy at the J_{th} scanning position. As stated earlier, this diffraction pattern only measures the intensity of the wave. The coherent diffraction intensity at a J_{th} scanning position can be expressed as

$$I_J(q,E) = \left|\mathcal{F}\psi_{(r)}^{j}\right|^2 \quad 1.12$$

Where $\mathcal{F}$ is the Fourier transform operator and q corresponds to the reciprocal space coordinate.[30,31] Hence, the phase retrieval process is an inverse Fourier transform calculated at each scanning position, to obtain the phase changes along with the amplitude (related to intensity changes or absorption) of the object.

There are many phase retrieval algorithms used to perform this calculation for ptychography data. The most common algorithm is the Ptychographical Iterative Engine (PIE), used by multiple codes (e.g. Scalable Heterogeneous Adaptive Real-time Ptychography, SHARP).[32] SHARP is used in this work, however, this thesis will not discuss in detail the theory behind the PIE algorithmic process. The important thing to note here is that ptychography provides information on the change in amplitude and phase after a wave transmits through an object. Figure 1.9 illustrates a simplified ptychography process used to generate a high-resolution real space image.

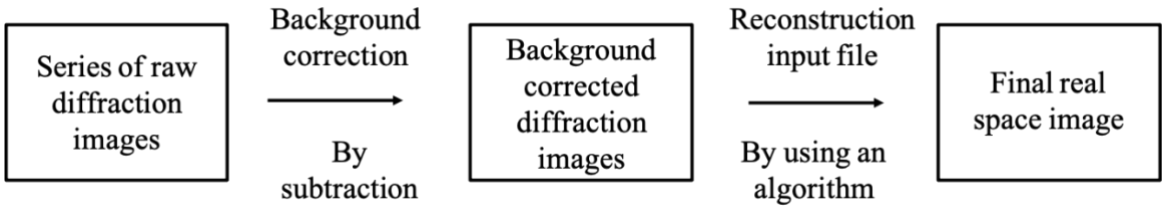

Figure 1.9. Ptychography data analysis procedure. Reciprocal space images (diffraction patterns) are reconstructed to amplitude and phase images with an iterative algorithm.

1.11.2 Spectro-ptychography

As the name implies, Spectro-ptychography involves a series of diffraction patterns recorded at each pixel and across a sequence of photon energies. The reconstructed real space images, now expected to be at a higher resolution than STXM, are then used to obtain spectroscopic information, similar to spectro-microscopy. This in turn means that spectra recorded at a higher resolution enhance the ability to characterize sub-nanometer samples.

Zhu *et al*. have demonstrated a spatial resolution of 7 nm at the Fe 2p edge in their study of individual cells in magnetotactic bacteria.[33] Also, Shapiro *et al*. achieved a spatial resolution of 3 nm in their study of test patterns, which can be compared to the resolution of the wavelength and numerical aperture limit of the detector (2.7 nm).[34] Both studies show the potential of spectro-ptychography for high-resolution imaging and chemical sensitivity. In this study, spectro-ptychography is used to study Fe nanoparticles, and to highlight the challenges faced when acquiring spectro-ptychography data at the spectro-microscopy beamline at Canadian Light Source (CLS).

1.12 Relationship between phase and absorption spectra

One of the benefits of ptychography is that the phase signal provides new information that complements NEXAFS measurements.[35] A phase shift occurs when the incident wave interacts with the object. Recall the complex transmission function shown in equation 1.11. This transmission function can be related to the refractive index in §1.2.2 as follows [30,35]

$$T(r,E) = exp\ (2\pi i(n(r,E) - 1) \cdot z(r)/\lambda) \qquad 1.13$$

where $z(r)$ is the local sample thickness, and λ is the wavelength of the illumination. From §1.2.2, the phase, δ and absorption information, β can be used to describe the complex refractive index of a sample. Therefore, the complex transmission function can then be written in terms of absorption or phase [30]

$$T(r,E) = exp\left(\frac{-2\pi}{\lambda}\beta(r,E)\ z(r)\right) \qquad 1.14$$

$$arg\ T(r,E) = \frac{-2\pi}{\lambda}\ \delta(r,E)\ z(r) \qquad 1.15$$

The phase and absorption can both be obtained experimentally with ptychography, and they can be related theoretically using Kramers-Kronig analysis on the dispersion of X-rays.

1.12.1 Kramers-Kronig integral

The Kramers-Kronig (KK) relationship can be used to calculate the phase shift δ from the absorption data β and vice versa. In other words, it relates the real and imaginary components of the atomic scattering factors f_1 and f_2 to each other (Equation 1.5). A simplified integral used to numerically calculate one component from the other is as follows

$$f_1(E) = Z + \frac{2}{\pi} P \int_0^\infty \frac{\epsilon\, f_2(\epsilon)}{E^2 - \epsilon^2}\, d\epsilon \qquad 1.16$$

Z is the atomic number, E is the photon energy, and ϵ is the integration photon energy. P is the Cauchy principal value since the integral is undefined at $E = \epsilon$.[36] This equation implies that a correct estimate of f_1 requires integration over an infinite spectral range. However, a typical absorption spectrum or 'f_2 data' obtained experimentally considers a finite spectral range to observe distinct features of the molecule, the absorption threshold region. It is, therefore, useful to examine the energy-dependent weighting term[8]

$$\kappa = \frac{\epsilon}{E^2 - \epsilon^2} = \frac{E + \Delta E}{-2E\Delta E - \Delta E^2} \qquad 1.17$$

κ describes the energy-dependent weighting of $f_2(\epsilon)$ in determining $f_1(E)$. Henke *et al.* have done work to build a database of tabulated atomic data, where the integral for $f_2(\epsilon)$ data over the range of $10 \leq \epsilon \leq 30\,000$ eV is used to obtain $f_1(E)$ over the range of $50 \leq E \leq 30\,000$ eV.[7,8] For calculation purposes, the near edge data is first spliced into the Henke atomic data of $f_2(\epsilon)$ and the integral is carried out to obtain a near edge determination of $f_1(E)$.[8] Figure 1.10 shows an example of the f_1, f_2 and Henke data.

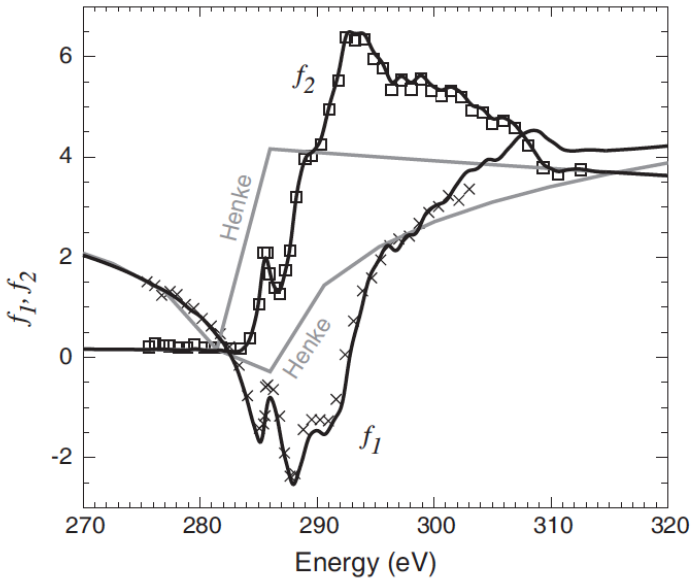

Figure 1.10. Comparison of f_1 values (using the amorphous carbon near edge f_2 data of Dambach et al.[37]) with experimental measurements of f_1. The boxes show the original f_2 values and the curve is the smoothed and spliced version of the same data to match Henke data. Figure reprinted from Jacobsen, with permission.[38]

1.13 Research objectives

The objective of this work is to develop methods to obtain single nanoparticle resolved NEXAFS spectra using spectro-ptychography. This work restricts itself to the use of iron oxide nanoparticles because they have a sharp core edge, the ptychography detector is sensitive to photons at the iron 2p edge energies, and well-characterized samples are available. Therefore, iron oxide is a suitable candidate to push the analytical limits of performing spectro-ptychography at the spectro-microscopy beamline at CLS.

Since ptychography can provide additional information on the phase changes, it becomes important to understand how the phase spectra compared to the absorption spectra. §1.8.1 points out that NEXAFS is useful for quantitative analysis, but the use of phase signals for quantitative purposes is not well understood. Nonetheless, phase contrast imaging is significant because it can provide imaging with a lower radiation dose than with absorption imaging, especially at photon energies where the absorption contrast is weak.[39] This is useful in cases where radiation damage is a concern.[34] This work will explore the phase spectra from spectro-ptychography results and use Kramers-Kronig integral to show the relationship between absorption and phase. The Kramers-Kronig integral is also used on experimental Fe 2p absorption spectrum for the following iron-based compounds: α-Fe_2O_3, γ-Fe_2O_3, Fe_3O_4, FeO(OH), $Fe_2O_3 \cdot 0.5H_2O$, $FeCO_3$, green rust, and oxidized green rust. Each of these absorption spectra was obtained from Dr. M. Obst[40] to calculate their corresponding phase spectra.

Lastly, this work will highlight the experimental and practical factors that affect spectro-ptychography, at the time of writing. It is important to point this out for a better understanding and appreciation of how spectro-ptychography data is acquired and processed at CLS. For example, the data analysis pipeline is constantly evolving and has been streamlined for easier use. This will ultimately play a role in improving the ability to work towards single nanoparticle spectro-microscopy.

The outline for the rest of this thesis is as follows: Chapter 2 is intended to cover experimental methods, Chapter 3 entails the results and discussion section, Chapter 4 concludes with the main contributions of this work, limitations, and future work on spectro-ptychography.

CHAPTER 2 EXPERIMENTAL AND METHODS

2.1 Sample preparation

Iron oxide nanoparticles used in all experiments conducted were obtained from US-Nano[41] and Nanocomposix.[42] The sample preparation described herein involves getting the purchased samples ready for soft X-ray spectro-microscopy analysis.

2.1.1 Iron(III) oxide Fe_2O_3

Size-specific iron(III) oxide dispersions (10 nm α-Fe_2O_3 and 30 nm α-Fe_2O_3 15 wt% in ethanol) were purchased from US-nano.[41] A portion of this solution was diluted to 0.1 % (w/v) in ethanol to ensure that the particles were monodispersed. The resulting diluted solution was sonicated for 45 min to 1 hr and a drop of the solution was cast on TEM grids and SiN_x windows.

2.1.2 Iron(II, III) oxide Fe_3O_4

20 nm Fe_3O_4 was also purchased from Nanocomposix.[42] Similar to the preparation of α-Fe_2O_3 samples, each solution was sonicated for 45 min and immediately cast on Formvar/C TEM grids for initial TEM images to identify sample areas. Spectro-ptychography results for this sample are not included in this work.

2.1.3 TEM survey

TEM imaging was conducted at the WCVM imaging center. A TEM survey was needed to locate sample areas before STXM-ptychography experiments. This allows us to be as efficient as possible due to the limited time available for measurements. A region can be identified with TEM to contain the sample in question and to ensure there are no artifacts. Also, the goal was to identify monodispersed particles to examine single nanoparticles with STXM-ptychography. Therefore, a TEM survey becomes useful to select a region with even distribution of nanoparticles.

2.1.4 Dynamic light scattering

Dynamic Light Scattering (DLS) was performed to further verify the size of the nanoparticles purchased. It is a useful tool in characterizing the sizes of many nanoparticles as it

gives an ensemble average based on diffusing particles. DLS results of α-Fe_2O_3 nanoparticles purchased from US-nano are included in the supplementary information.

2.1.5 Mounting sample on a STXM sample plate

After confirming the presence of nanoparticles and choosing a specific region with TEM, the TEM grid or SiN_x window was mounted on a calibrated STXM sample holder (Figure 2.1). The sample was then previewed with an optical microscope before the beamtime experiment. The following experimental sections describe the procedure for a STXM-ptychography setup.

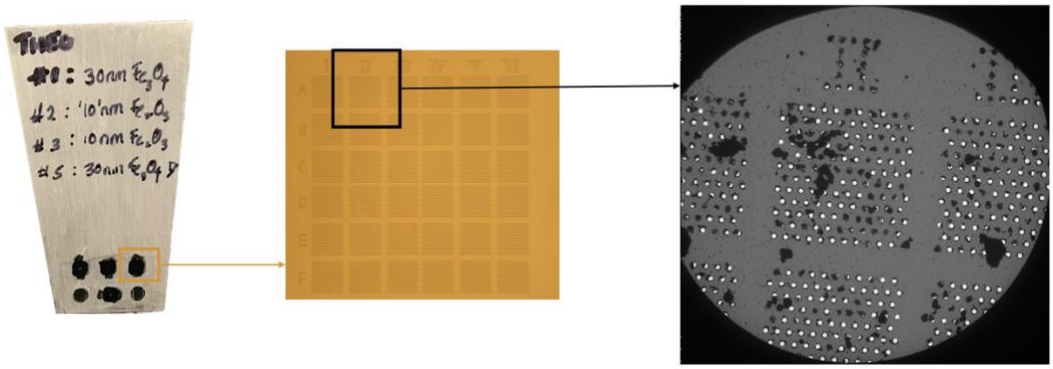

Figure 2.1. Left. Location-tagged SiN_x membrane (50 nm thick and 0.5 x 0.5 mm window size) on a STXM sample plate. Middle. Close-up of holey patterns on SiN_x membrane (2.0 µm hole size). Right. TEM image showing α-Fe_2O_3 nanoparticles.

2.2 Spectro-microscopy beamline

All experiments were performed at the spectro-microscopy, SM beamline at Canadian Light Source, CLS using an elliptically polarized undulator EPU source. The same spectro-microscopy facility was used for both ambient STXM and ptychography measurements. The end station of this beamline consists of photon shutters, a plane grating monochromator, Fresnel zone plate focusing optic, an order sorting aperture, and a sample plate to hold the sample in position (Figure 1.6). In the case of STXM measurements, a scintillator coupled with a photomultiplier tube PMT was used as the detector. Ptychography required the use of a charged coupled device CCD as the detector.

The STXM microscope at the SM beamline is controlled by the STXM branch Graphical User Interface (GUI) and the STXM control software on the STXM control computer (S.I. Figure 5.1). The STXM branch GUI can be used to open/ close the SM photon and beam shutter to allow/ block X-rays from going further down the beamline. It can also be used to select a

specific edge, energy range, polarization, and other parameters to optimize the microscope for measurements. The absorption edge selected for Fe 2p is 710 eV and a circular left polarized light was used for all measurements. Other scan parameters are included in the supplementary information (S.I. Table 5.1 andTable 5.2).

2.2.1 STXM setup

The sample was mounted in the STXM chamber, and the chamber was then pumped to a rough vacuum (~ 0.2 torr). The microscope was calibrated along with a series of OSA, detector, and focus scans to ensure the sample was in focus and optical elements were aligned. The goal here was to make sure the beam was fully optimized for STXM-ptychography measurements. STXM was used to locate a sample region in focus. This region was intended to act as a template for further experiments with ptychography mode. Once a suitable template was found, the PMT detector was switched to a charged coupled device (CCD) to obtain ptychographic results.

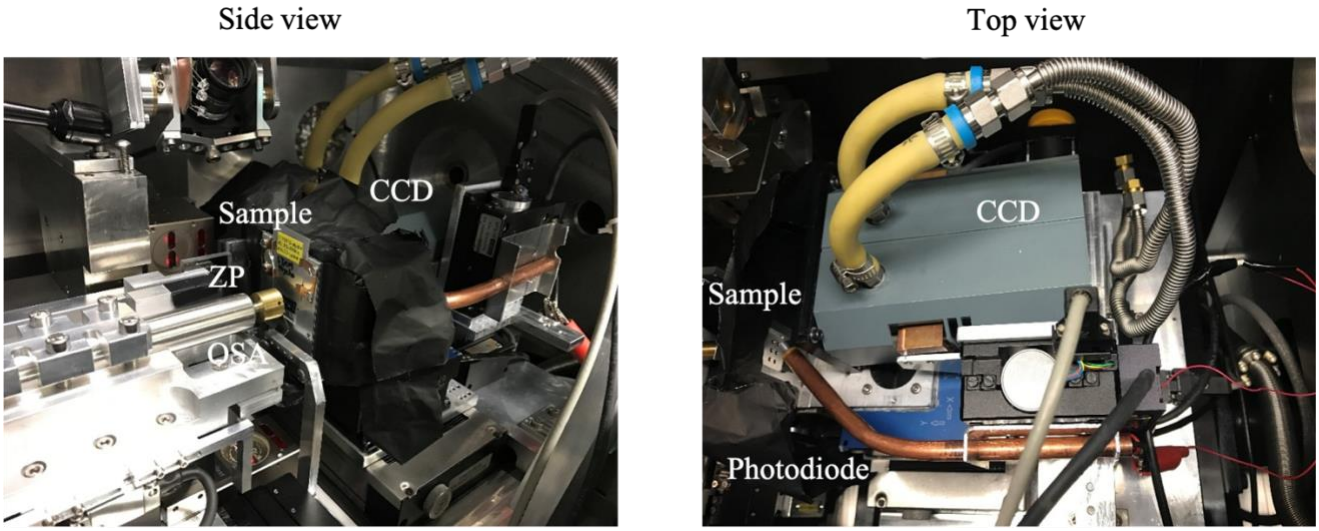

Figure 2.2. Top and side view of STXM-ptychography set up at the spectro-microscopy beamline, CLS. Image courtesy of Dr. J. Wang.

2.2.2 STXM-ptychography

Ptychography at the spectro-microscopy beamline uses the scanning capability of STXM, hence it can be referred to as STXM-ptychography. A specially designed ptychography OSA with 30 µm holes and a 40 nm zone plate was used for experiments. Once ready to switch to ptychography imaging, the STXM-ptychography chamber was pumped to a higher vacuum than in conventional STXM. Also, the shutter control cable was changed so that the shutter signal was

used as the trigger for CCD imaging. The STXM software controls the piezo shutter on the beamline to limit users to radiation exposure.

2.2.3 CCD camera

A pixel or image sensor is required to capture the diffraction patterns in ptychography. In this work, 1024 x 1024-pixel Andor CCD or 2048 x 2048-pixel GreatEyes CCD camera was used to capture each diffraction pattern in a step scan mode. The CCD image sensor collects scattered photons in pixels, and the photons create electric charges that are read as analog voltages. The voltages are converted to digital values and processed to form a visible image.

A water-cooling system was in place to lower the temperature of the camera to -40° C which reduces camera noise (Figure 2.2). Most of the results shown herein use the Andor camera, however, some beam time experiments involved the use of the GreatEyes camera on the cryo-STXM. The software operated for these cameras was the Andor Solis or the GreatEyes Vision 8.0 packages.

2.3 Ptychography data acquisition

2.3.1 Single image

A typical ptychography scan involves the simultaneous operation of the CCD software and the STXM control software. The CCD camera is used to record a series of diffraction patterns at locations determined by the STXM control software. The time it takes for the camera to acquire and transfer data must match the sample scan pixel rate on the STXM control. Hence, the camera data acquisition is triggered at each pixel position, through the trigger control. For a camera dwell time or exposure time of 800 ms (actual data acquisition time), a STXM control dwell time of 3000 ms was used to account for the measurement and data transfer time. Challenges with the data acquisition and synchronization process will be discussed in §3.5.1.

2.3.2 Data redundancy in ptychography

In ptychography, the selected region is raster-scanned in such a way that each diffraction pattern at a single-pixel overlaps with that of the adjacent scanning spot. This helps to ensure convergence of the iterative reconstruction process. Therefore, the overlap condition is important to note before starting any step-scan measurement. Figure 2.3 illustrates the overlap of diffraction patterns required for the iterative process described in §2.4. A background image was

obtained by measuring in the absence of the beam. The detector software automatically corrects for counts by subtracting this pre-recorded background image.

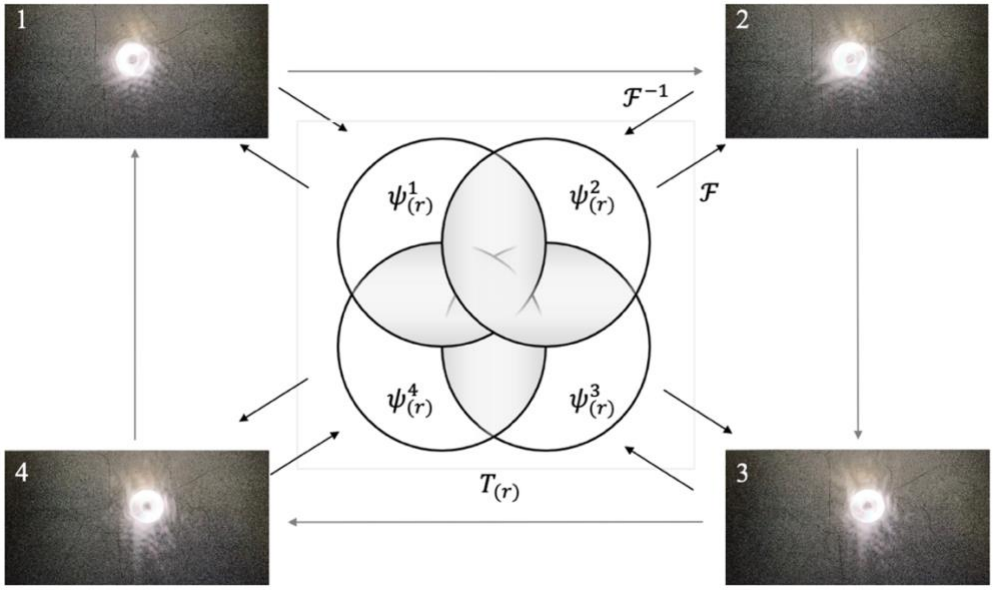

Figure 2.3. Schematic of 4 overlapping diffraction patterns (step size = 0.05 µm). Arrows between each diffraction pattern represent the scanning direction. Other arrows describe the iterative process between the Fourier space and real space to find the complex-valued transmission function, $T(r)$ at single energy (710 eV). Image concept adapted from Pfeiffer F.[31] with data used in this thesis.

2.3.3 Spectro-ptychography

For spectro-ptychography, an image 'stack' (a sequence of ptychographic image datasets) was measured at a series of different energies. A fine scan (closer energy spacing) was performed at energies where we expect to see detailed spectral features (0.2 – 0.5 eV). At other regions in the spectrum, the energy interval for image acquisition was 1 – 5 eV. Hence, a coarse scan was performed at these regions. In doing so, the beam time was managed effectively while still providing relatively well-resolved spectra. Figure 2.4 illustrates the fine and coarse energy ranges using literature NEXAFS spectra of Fe_2O_3 obtained from Dr. M. Obst.[40]

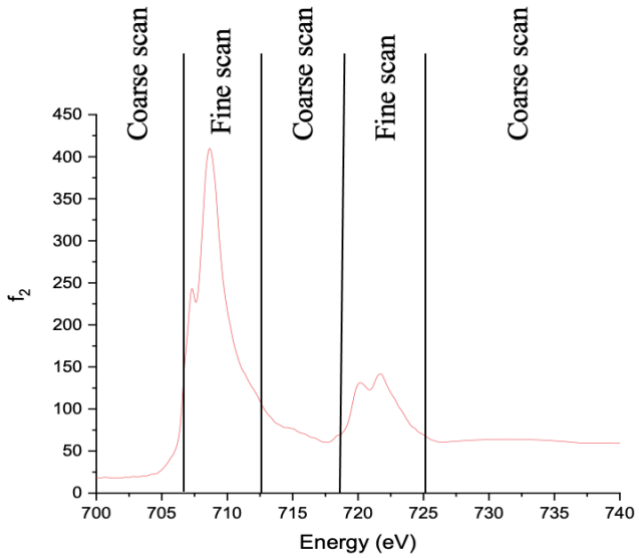

Figure 2.4. Figure indicating the regions for fine and coarse ptychography image scans in Fe $L_{2,3}$ edge NEXAFS region. Dr. M. Obst, private communication.[40]

2.4 Data processing

The process of reconstructing diffraction images to real space images can be very tasking. The fundamental problem consists of finding the correct phases that go along with the measured intensities, such that together they can be Fourier transformed into real space images.[32] In this work, a SHARP code[32] based on the ptychographic iterative engine (PIE) algorithm was implemented at the CLS by Dr. J. Wang and Dr. Y. Hao. SHARP is an open-source software package that can be used to solve ptychographic problems (phase retrieval problems).

The iterative process carried out by the SHARP code started with a random initial guess of the object $T_0(r)$. Other input data included were the initial illumination $P_0(r)$ and a Fourier mask used to refine the illumination.[32] The estimated object was then Fourier transformed $\psi_0(q)$, and the Fourier transform was made to conform to the known intensity.[43] In other words, the intensity distribution or diffraction of the random object was replaced with the experimental diffraction (i.e., the model). This updates the exit wave from the object to give $\psi_1(r)$ and the process is continued until convergence (Figure 2.5). In much simpler terms, the code was used to calculate a series of Fourier and inverse Fourier transforms until the magnitude of the overlap error was small.

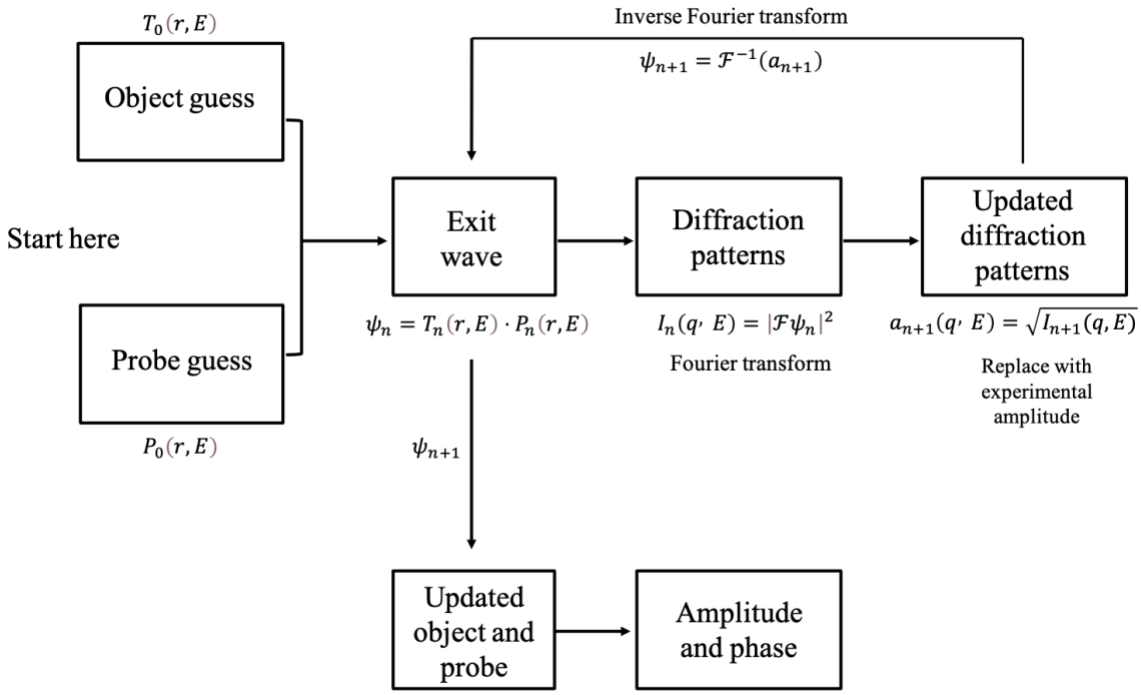

Figure 2.5. Ptychography iterative phase retrieval process. *I* and *a* denotes intensity and amplitude respectively. Image concept adapted from Sun, T., *et al.*[44]

In practice, the phase retrieval process in ptychography is usually performed offline after the data acquisition, which may be a few days after beam time experiments. This is unlike many other microscopic techniques where the sample is imaged in real time, and adjustments can be made to improve the image resolution. Here, acquiring diffraction images allow the potential for higher resolution images but it can be tedious to reconstruct each image while collecting raw diffraction images. Ideally, the images are reconstructed simultaneously with data acquisition for better navigation to ensure the scan focuses on the sample area. This is currently not the case for STXM-ptychography experiments at CLS. Also, the ptychography phase retrieval process can result in reconstruction image artifacts, and if this happens the experiment will need to be repeated at the expense of time (§3.5.6). The reason for a reconstruction output with artifacts is unclear and requires a good understanding of how the PIE algorithm works. One of the research objectives in this thesis is to first understand what does not work and highlight any inefficiency in ptychography data analysis. This will help bridge the knowledge gap between developers and everyday users.

Figure 2.6 shows a schematic of the ptychography data flow between each computer used to acquire and process data. After acquiring data during a beam time shift, the diffraction images

were transferred from the STXM computer to a high-performance computer (ptychography workstation at SM beamline) for data processing. This computer is ideal for handling ptychography data as it consists of an 8 core CPU for its processing capability and 6GB GPU for parallel computing. Data pre-processing code was first used to convert between data file formats (§2.5). After this, the SHARP code then reconstructs the data to give an amplitude and phase image. Note that the amplitude is related to intensity as indicated in Figure 2.5.

The SHARP code was executed using Spyder, an open-source python development environment for scientific programing. When running the SHARP code on Spyder, the amplitude and phase image can only be reconstructed for diffraction patterns acquired at a single energy. Therefore, this process was repeated for each energy point in a stack data. §2.6 discusses the data analysis performed to obtain spectro-ptychography data.

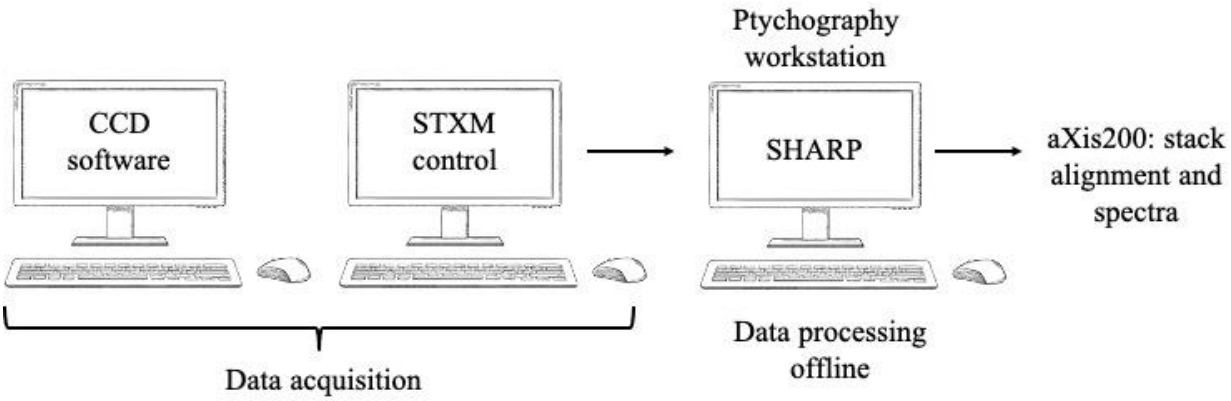

Figure 2.6. Ptychography data flow from data acquisition to data processing and to image stack alignment and spectra (spectro-ptychography).

2.5 Data formats

Each of the steps shown in Figure 2.6 results in a different file format used as the input file for the next step. This section is intended to cover the data formats used for each step of the data acquisition, data pre-processing/ processing, and analysis. The camera saves the diffraction image in a *.fits* file format. This diffraction image serves as the file input for pre-processing, along with a background image *.bg*, and a STXM *.hdr* file, which contains scan metadata. This data was pre-processed to an input *.cxi* file for SHARP, and then the final reconstructed output was in *.jpg* and *.tif* format. The *.tif* amplitude and phase image output was useful to manually obtain the spectroscopic information using aXis200 software.[45] This manual process involved setting the x,y scale, energy, dwell time, and changing the mesh for each amplitude and phase

image. The resulting images were written in *.axb* (aXis format). Amplitude and phase images were arranged into separate stack list *.sl* input file. This input file was saved as an image sequence in binary format *.ncb* for further analysis.

2.6 Obtaining a spectrum from reconstructed image stack

The process of obtaining a spectrum was performed using the un-compiled version of aXis2000 software[45] running on IDL versions 8.1- 8.7. This software was used for viewing and processing X-ray microscopy images, spectra, and stacks. The amplitude image stack was aligned using aXis2000 autocorrelation routine (ZSTACK align), where each preceding image was used as a reference image for alignment. After this step, the alignment shift *.aln* file from the amplitude image stack was applied to the phase image stack. Both aligned and trimmed stack files were saved as *a.ncb* aXis binary format, where *a* denotes that the stack file was aligned. Absorption and phase spectra were extracted from the aligned amplitude and phase image stacks respectively by using a stack process script on aXis2000. All absorption spectra shown in this work are in optical density (OD). The optical density spectra were obtained using Beer's law by defining I_0 and I regions in the image. The phase spectra measure the phase shift, and both absorption and phase spectra are presented without normalization.

2.7 Kramers-Kronig relations

The process of calculating the phase data f_1 from absorption data f_2 was carried out using the *KK_gui* program created by Dr. C. Jacobsen.[8] Any noise from the data was first filtered out by applying a Fourier filter to each spectrum. The next step involved numerically calculating f_1 with the Kramers-Kronig integral shown in equation 1.16. Kramers-Kronig analysis was performed on NEXAFS of iron oxide compounds from Dr. M. Obst.[40] and on the measured iron(III) oxide absorption spectrum in spectro-ptychography. The NEXAFS data obtained from Dr. M. Obst[40] was normalized by matching each spectrum to the Henke atomic photo-absorption cross-section (see Figure 1.10). Once the NEXAFS data was normalized, the *KK_gui* code was used to estimate the phase signal for each iron-based compound. To further test the Kramers-Kronig transform, the measured absorption spectrum from spectro-ptychography was used to calculate another phase spectrum. These results are presented at the end of chapter 3.

CHAPTER 3 RESULTS

3.1 Characterization of purchased FeOx nanoparticles

TEM results of iron oxide nanoparticles purchased are shown in Figure 3.1. It is important to characterize the samples purchased and to make sure they are in fact what was intended for the experimental design in this work. TEM results indicate that the nanoparticles form aggregates.

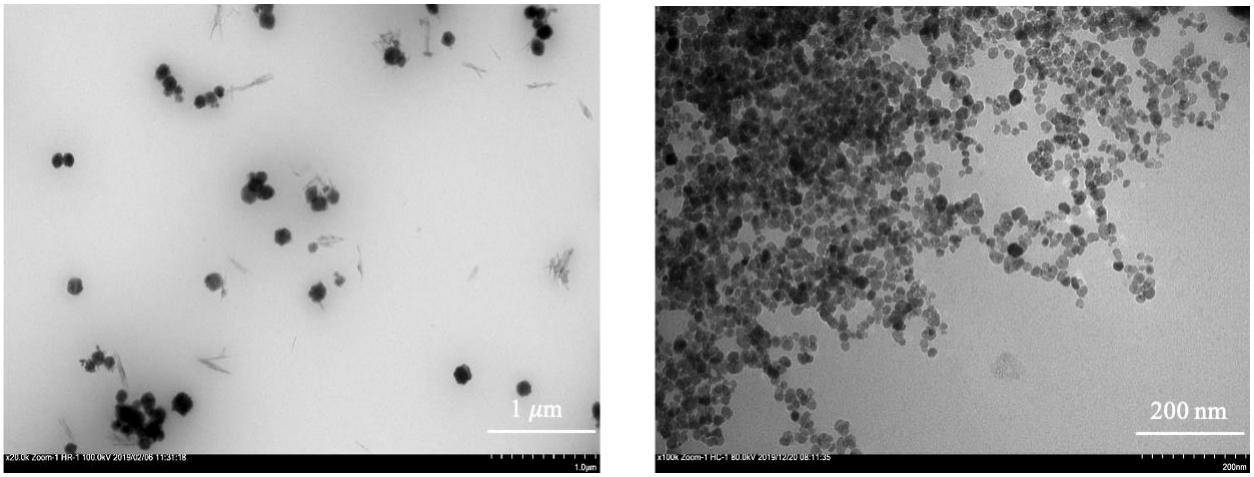

Figure 3.1. Left: TEM image of 10 nm α-Fe_2O_3 aggregates. Right: TEM image of 20 nm Fe_3O_4 aggregates. The nano-rod structures are not of any particular interest here and are a result of nanoparticle synthesis.

In this work, we demonstrate spectro-ptychography with these nanoparticle aggregates as they are easier to measure than isolated nanoparticles. This is a step towards realizing the broad goal to measure systems that are well mono-dispersed and identify the analytical limit of spectro-ptychography. Measuring single nanoparticle resolved spectro-ptychography is currently a challenge due to the spatial resolution limit in STXM (with the use of a 35/ 40 nm ZP). Since STXM is first used to find suitable regions for ptychography imaging, it can be difficult to find and focus on smaller sized nanoparticles. This is especially the case for nanoparticles smaller than the typical resolution in STXM. As mentioned in the experimental section of chapter 2, a TEM survey before ptychography measurements can be useful to help navigate sample areas not well resolved with STXM. Location-tagged TEM grids or SiN_x membranes helps to re-locate a suitable region of interest.

3.2 STXM survey of α-Fe_2O_3 nanoparticles

All STXM images were acquired at 710 eV, which is the maximum of the Fe 2p 3/2 absorption band, and with a dwell time of 1 ms. The dwell time of the scanning probe is routinely set to 1 ms at the SM beamline because of mechanical limitations – the piezo scanning stage is unable to move faster effectively. As will be later discussed in §3.5.2, the scanning speed is critical in obtaining measurements, particularly in the case of spectro-ptychography. Figure 3.2 shows a STXM image of α-Fe_2O_3 nanoparticle aggregates using a 40 nm zone plate. Although the nanoparticle aggregates are easily visible with STXM, individual nanoparticles cannot be resolved. Nonetheless, the highlighted region is selected for further imaging with ptychography to record higher spatial resolution images.

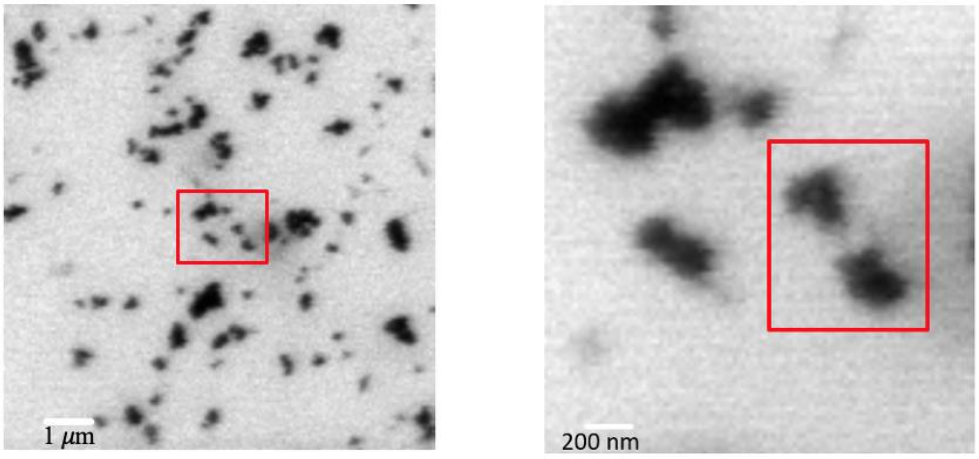

Figure 3.2. Left. 10 x 10 μm STXM image obtained at 710 eV and 1 ms dwell time. Right. The selected region in red highlight is viewed with ptychography.

3.3 Single energy ptychography scan on α-Fe_2O_3 nanoparticles

Figure 3.3 shows a single diffraction image captured by the CCD detector during ptychography data acquisition at 710 eV. However, a ptychography dataset consists of multiple diffraction images recorded at each pixel in a ptychography scan. These diffraction images are reconstructed together to give the amplitude and phase image. Ptychography results show higher spatial resolution when compared to STXM images of iron(III) oxide NP's at the same region (Figure 3.2). The ptychography amplitude and phase image also show some reconstruction artifacts along the y-axis. Image artifacts may occur from reconstruction, and this is one of the challenges faced when processing ptychography data. Challenges in acquiring and processing ptychography data are discussed in detail in §3.5.

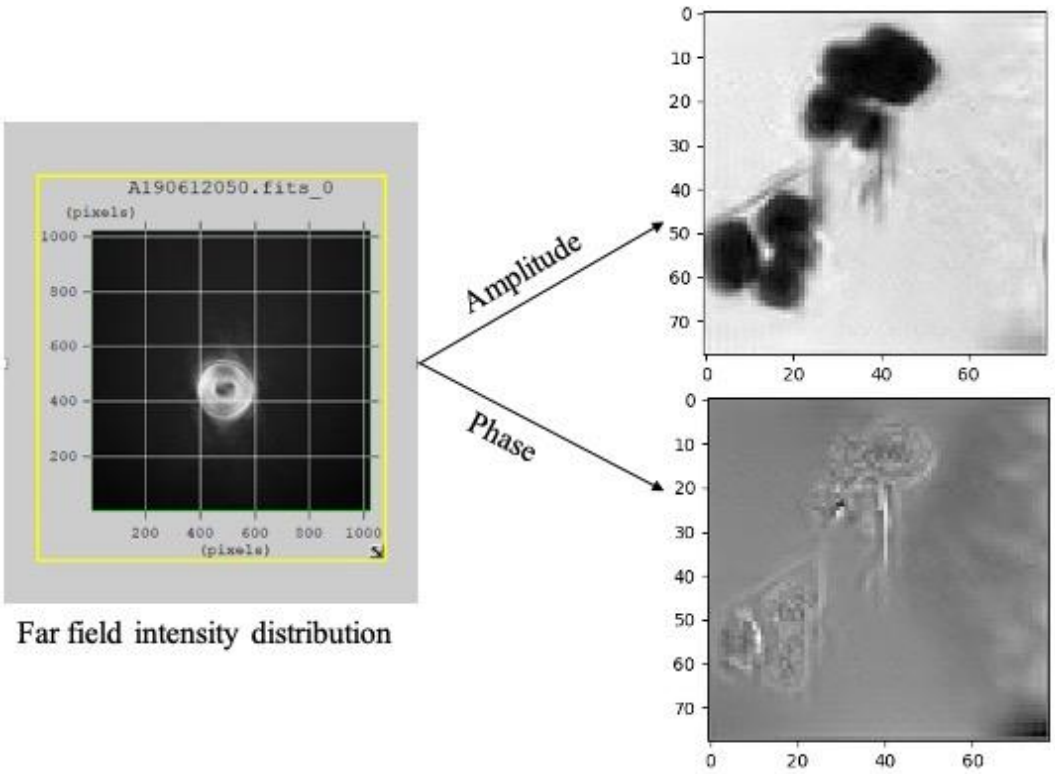

Figure 3.3. Left. A snapshot of a single diffraction pattern. Right. The amplitude and phase images were obtained via reconstruction of overlapping diffraction patterns within the scanning region of 0.8 x 0.8 μm, 16 x 16 pixels, and with a dwell time of 2300 ms.

3.4 Spectro-ptychography on α-Fe_2O_3 nanoparticles

In spectro-ptychography, a sequence of ptychography images at different energies is acquired to obtain spectroscopic information. Figure 3.4 shows spectro-ptychography images at 7 energy points near the spectral features between 700 eV and 712 eV. There is a change in contrast at 710 eV in both the amplitude and phase images, corresponding to the maximum in the Fe 2p3/2 edge. Data acquisition of 7 energy points is fast to acquire, but it does not provide much information for spectroscopy, therefore, more energy points are desirable. However, this is a trade-off between data completeness, acquisition time and data processing complexity. Some studies have performed spectro-ptychography over the full energy range of Fe $L_{2,3}$ absorption and phase spectrum.[34,46] For example, Zhu *et al.*[33] performed a ptychographic scan from 700 – 732 eV with 76 energy points, which provides a high-resolution absorption and phase spectrum. In this work, we measure up to 30 discrete energy points for spectro-ptychography (Figure 3.5). This measurement was performed at another region of interest using the same α-Fe_2O_3 NP aggregates but prepared on a different SiN_x membrane.

The measured absorption spectra from spectro-ptychography with 30 energy points are in good agreement with the literature α-Fe_2O_3 NEXAFS spectra.[16] The shoulder peak observed at 708.5 eV and an intense peak at 710.5 eV correspond to the t_{2g} and e_g ligand field splitting respectively. The phase spectra show the minimum signals at 708 eV and 710 eV similar to the multiplet effects in the NEXAFS spectrum (Figure 3.5).

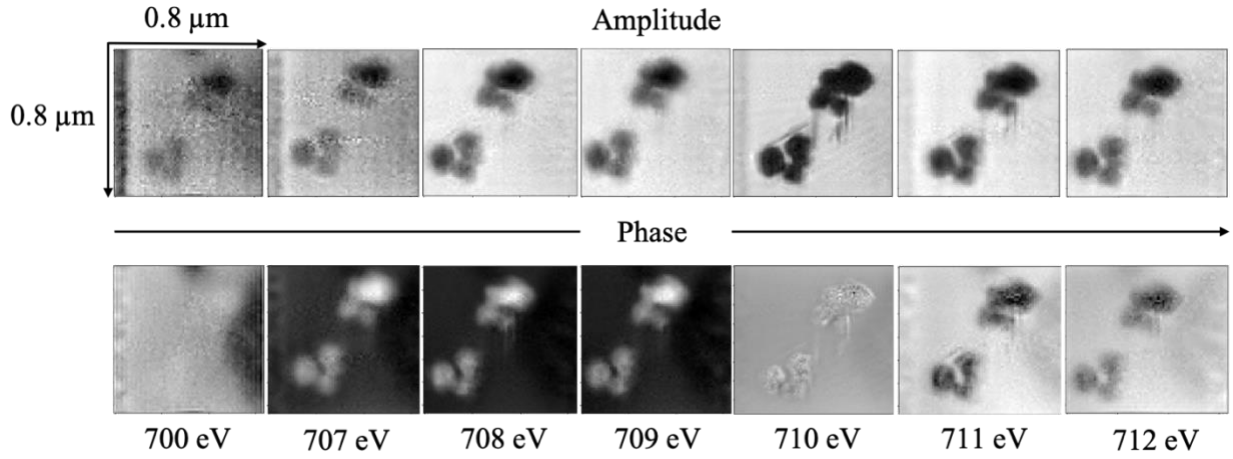

Figure 3.4. Amplitude and phase images from spectro-ptychography at 7 discrete energy points. Ptychography data acquisition on 06/19 with a scan size of 0.8 x 0.8 µm, 16 x 16 pixels, and a dwell time of 2300 ms.

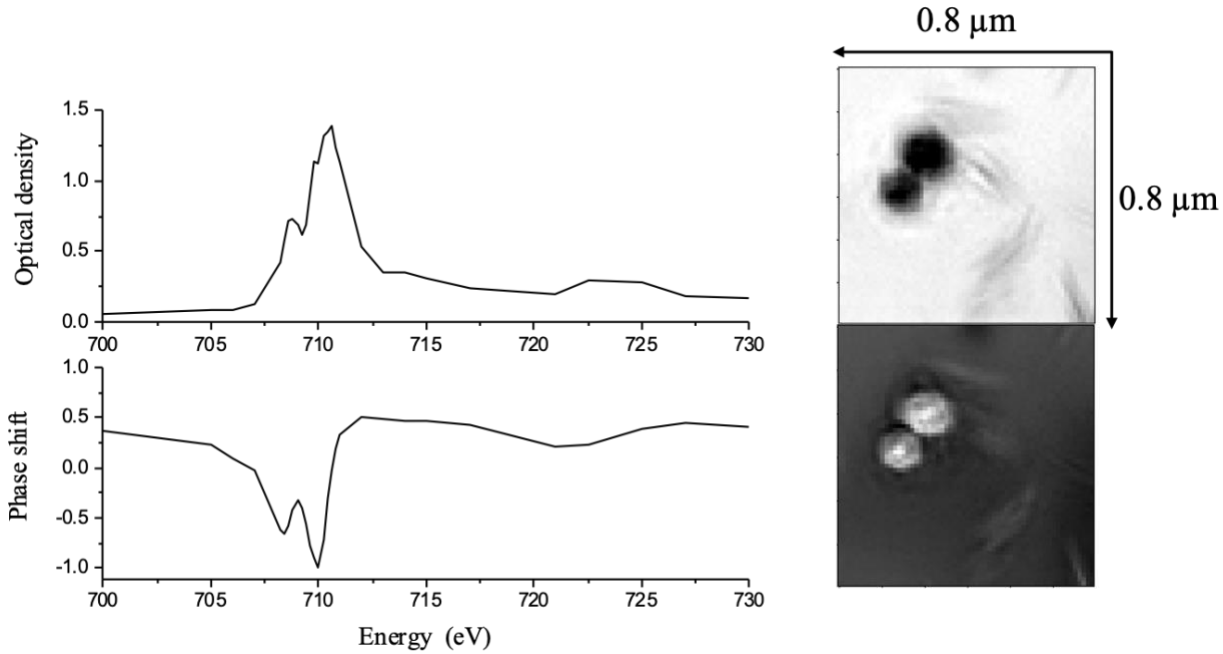

Figure 3.5. Left. Fe 2p absorption and phase spectra obtained from a stack with 30 discrete energy points. Right. Amplitude and phase image at 710 eV. Ptychography data acquisition on 08/20 with a scan size of 0.8 x 0.8 µm, 16 x 16 pixels, and a dwell time of 2300 ms.

3.4.1 Amplitude and phase spectra obtained from a single pixel

Spectroscopic information can be determined from a region of interest as small as a single pixel in an image stack. In this section, we examine the spatial resolution of spectro-ptychography data by observing differences in spectra from regions around iron(III) oxide nanoparticles. Figure 3.6 and Figure 3.7 both show that the further away from the center of the nanoparticle, the weaker the absorption signal. This is expected for absorption within a spherical structure, where the edge of the sphere may absorb less than the center. The expanded spectra focusing on 2p L_3 edge do not show any significant difference in spectral features, thereby indicating that there is no difference in chemistry but rather in the amount of material. Similar observations were made for the phase spectra extracted at regions around the particle. The author acknowledges that spectro-ptychography with 30 energy points does not result in a well-resolved Fe $L_{2,3}$ absorption or phase spectrum, and multiplet effects may be better observed by obtaining a stack of images with more energy points. §3.5.4 will discuss challenges in acquiring a stack and other factors that hinder the ability to obtain higher resolution spectro-ptychography data.

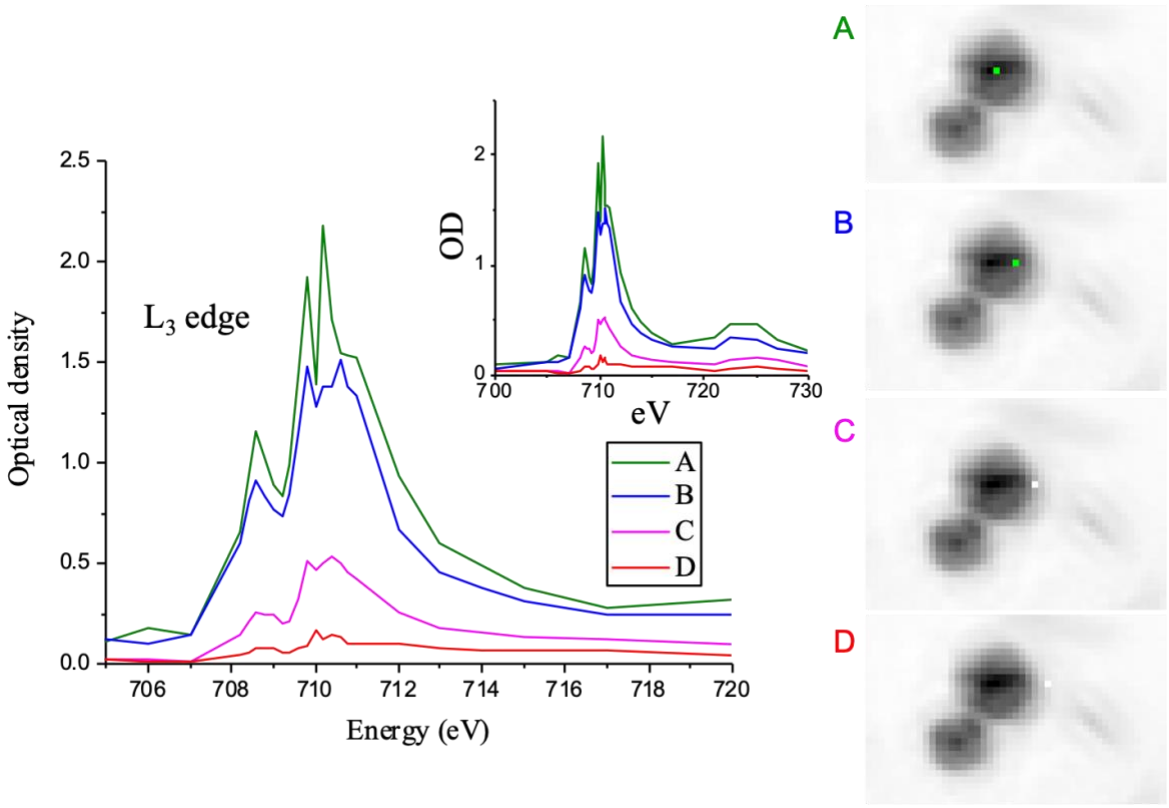

Figure 3.6. Single-pixel absorption spectra from the center of the particle to the edge. Expanded plot showing the L_3 edge, while the inset shows full range of iron(III) oxide NEXAFS spectra.

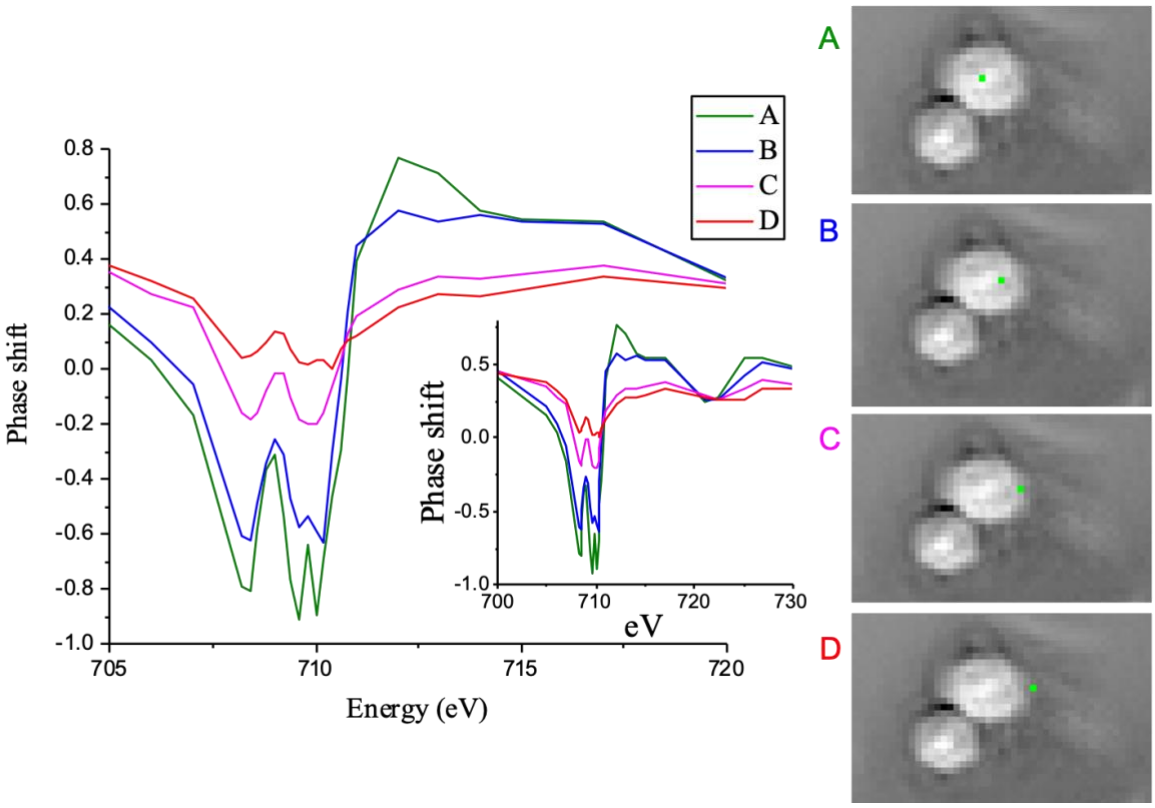

Figure 3.7. A. Single-pixel phase spectra from the center of the particle to the edge. Expanded plot showing the phase shift at the L_3 edge, while the inset shows the full range (700 – 730 eV) of the phase signal measured for iron(III) oxide.

3.5 Practical challenges in single nanoparticle spectro-ptychography

This section highlights the challenges encountered to obtain spectro-ptychography data at the time of measurement. Some of these challenges have now been resolved and improvements are made to ensure a user-friendly experience.

3.5.1 Data acquisition and synchronization

As mentioned in §2.3.1, the sample scan on the STXM control software must match the data acquisition by the CCD camera. The STXM control software has a dwell time for each ptychography scan that is typically set to 3000 ms when using the GreatEyes CCD camera. This includes the dwell time of the camera or exposure time which is 800 ms. Also, the camera requires some time to transfer data, in this case, a single diffraction image at a single-pixel position before recording the next diffraction image. We observed triggering issues between the STXM control and the GreatEyes CCD software due to this read-out time such that it was unstable for longer measurements. In other words, the data acquisition process between both

programs was not well synchronized because of the CCD read-out time. This issue was resolved by allowing a point delay time of 2999 ms to account for the read-out time of the GreatEyes CCD camera. Therefore, resulting in a total duty cycle time of about 6000 ms for a single diffraction image. Figure 3.8 illustrates the data acquisition profile between the STXM control software and the GreatEyes CCD.

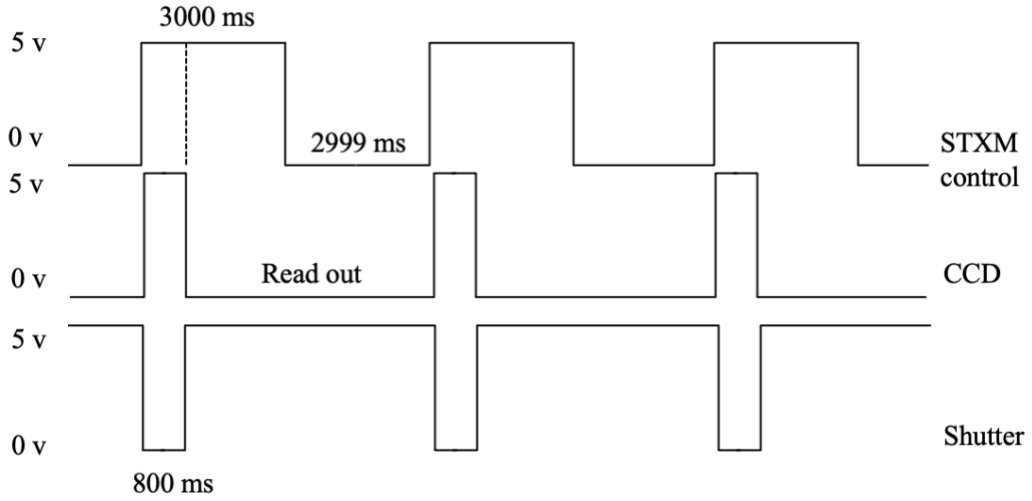

Figure 3.8. Schematic of the data acquisition between the STXM control, the GreatEyes CCD camera, and the shutter.

3.5.2 Scan speed vs spatial resolution

The step scan mode (also referred to as move-settle-measure mode)[47] for data acquisition can be time-consuming, especially when measuring at multiple energy points. In this work, it can take approximately 2 hours for 1600 measurements, which is a 10 x 10-pixel image recorded at 16 energy points, with a total dwell time of 4600 ms per pixel using Andor CCD camera. As shown in Figure 3.8, the CCD takes a significant amount of this time to read and transfer data, when the signal is not acquired. Hence, a point delay is necessary by the STXM control to prevent any loss of information, which may impact the spatial resolution of the reconstructed image. In this case, either the scan speed or the spatial resolution is compromised.

Recent work in other studies has implemented ptychography in fly scan mode.[48,49] In this mode, the probe is continuously scanned across the sample without collecting data at discrete positions, unlike a step scan measurement.[50] This can dramatically speed up data acquisition whilst providing high-quality images.[47] Although, a continuously moving sample creates blurry diffraction patterns,[48] its impact on spatial resolution is accounted for during the reconstruction

process. The reduction in the time it takes for data acquisition may enable studies of dynamics and in situ processes as well as reducing stability requirements on experimental components.[50] This approach was not used in this work, but represent a future direction in obtaining spectro-ptychography data efficiently (§4.5.1).

3.5.3 Mechanical instabilities

Instrument stability is an important factor to consider when measuring a stack of images. A common problem that occurs during a ptychography measurement is that the OSA pinhole starts to slowly drift away from the center of the beam. When this happens, the OSA needs to be re-positioned to prevent it from interfering with the beam and reducing coherence due to beam scattering. It is also possible for the sample to drift away from the scanning region while measurements are taken. This is due to the mechanical instabilities of motion controllers like the piezo stage. Figure 3.9 shows the sample drifting from the selected scanning region as the measurement is repeated at increasing energy points. Sample drifts can affect the quality of the data and the ability to perform accurate reconstruction of diffraction images. A solution to this problem is to increase the scan size so that the scan itself is larger than the drift. However, this increases the time it takes to acquire ptychography data.

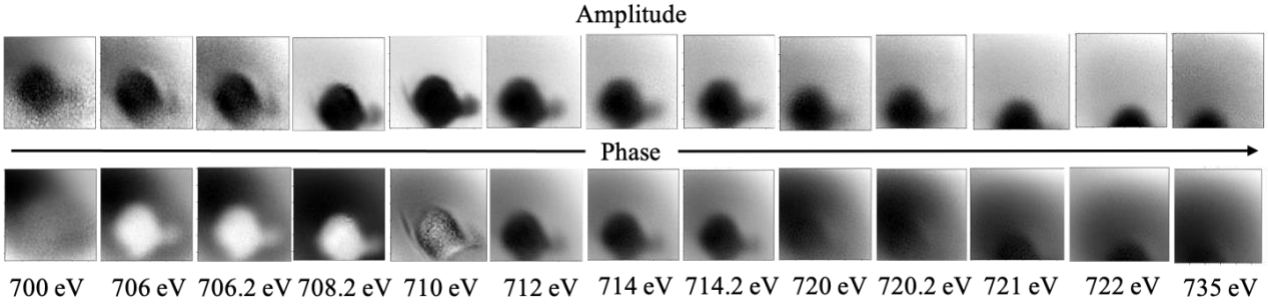

Figure 3.9. Sample slowly drifts away from the scan region as ptychography measurements are repeated at increasing energies.

It should be noted that the instruments become more stable during an extended experiment, as the mechanical instruments reach thermal equilibrium. In STXM, the STXM chamber is pumped to about 0.2 torr allowing convection to cool piezo stages and bringing other components to thermal equilibrium faster. However, in ptychography experiments, thermal equilibrium is slower because the chamber is pumped to 10^{-5} torr to prevent ice build-up on the

Peltier cooled CCD camera and minimize the loss of X-ray signals. Therefore, instrument drift occurs until its thermal equilibrium is reached.

3.5.4 Manual stack acquisition

Spectro-ptychography requires images to be reconstructed at multiple energy points to obtain an image stack and extract spectra. Although it is possible to set up the acquisition of a stack automatically, it is very important to first test the reconstruction process at single energy. Once it is confirmed that the sample region can be reconstructed to amplitude and phase images, then a stack measurement can be performed with confidence. The challenge here is the requirement to test the reconstruction process at each energy. This can become very tedious from the perspective of a user who intends to quickly acquire high-resolution ptychography images of the sample in question. The short-term goal is to optimize experiments to obtain diffraction patterns and reconstruct images simultaneously. This ensures that the image can be reconstructed successfully and if this is not the case, another scan can be performed.

3.5.5 Processing ptychography data

Ptychography measurements result in a large amount of data. As an example, it may take up to 400 diffraction patterns (frames) to generate a single 20 x 20-pixel image. This requires a computer with many GPUs that allow for memory storage during processing. At the time of writing, the raw diffraction images are transferred to a separate ptychography computer for reconstruction (§2.4). The transfer of data between computers and the data analysis pipeline has been streamlined for easier use.

Another challenge is that the reconstruction process needs to be performed manually for each energy point when using the SHARP code. However, this has been addressed by switching to pyPIE[44] for current and future data processing of raw diffraction images. The new pyPIE software for the SM beamline was developed by T. Sun and Dr. J. Wang, which is based on the PIE algorithm for ptychography analysis.[44] This software will enable a one-time reconstruction of a sequence of images at different energies to give the individual amplitude and phase images.

3.5.6 The risk of image reconstruction artifacts

Image artifacts may exist in the reconstructed image and prevent our ability to characterize samples. Figure 3.10 shows image artifacts present in an amplitude and phase

image. The cause of these artifacts is not well understood but is related to the phase retrieval algorithm used. This further emphasizes the need for real time image processing to repeat experiments when reconstructed images are unsatisfactory.

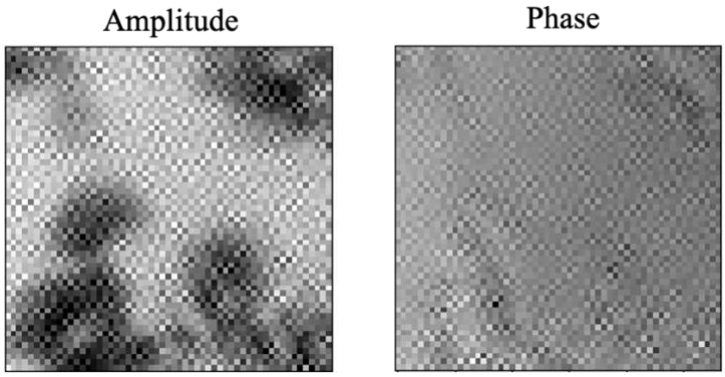

Figure 3.10. Reconstruction artifacts in amplitude and phase images of α-Fe_2O_3 NP aggregates obtained with SHARP code. Ptychography data acquisition at 710 eV with a scan size of 0.3 x 0.3 µm, 10 x 10 pixels, and a dwell time of 2800 ms.

3.5.7 Obtaining spectra from ptychography images

As mentioned in chapter 2, spectra were obtained using aXis2000 software. In this work, this process was performed manually by first defining the x, y scale, energy, mesh and dwell time for each reconstructed *.tif* output image. This was necessary because the SHARP code used does not support energy range definition. After selecting the appropriate image property, all images were arranged in a list for image stack alignment described in §2.6. Setting the information for each image can be time-consuming and limits the ability to quickly generate a well-resolved spectrum with multiple energy points.

3.6 Kramers-Kronig analysis of NEXAFS data

Radiation damage can occur to radiation-sensitive materials, which may affect the resolution obtained in absorption mode.[8] However, several studies have proposed the potential for phase-contrast imaging to enable measurements at a lower radiation dose.[39,51] This is explored in this work, where the phase contrast is observed at photon energy lower than the absorption edge. Phase spectra could also be relevant for quantitative analysis and chemical differentiation if the relationship between spectra and composition is well understood. This section will use Kramers-Kronig analysis to compare the absorption and phase information from spectro-ptychography. The author of this thesis used Dr. C. Jacobsen's *KK_gui* code[8] with iron-

based compounds, to learn how to calculate the phase spectra from given absorption spectra. The absorption spectra used for this test were obtained from Dr. M. Obst.[40]

3.6.1 Absorption vs phase spectra

As mentioned in chapter 1, the absorption and phase information can be related to each other with Kramers-Kronig integral (Equation 1.16). First, the Fe 2p spectra of common iron-based compounds was normalized to the Henke cross-section. Once normalized, Kramers-Kronig integral was used to numerically determine the phase spectra f_1 from the absorption spectra f_2 (Figure 3.11 below).

All iron oxide 2p NEXAFS spectra show similar spectral features since iron-based compounds have similar chemical characteristics (Table 3.1). Our focus is on the L_3 edge because the narrow and sharp absorption band is easy to observe. The subtle difference between the intensity of both peaks at the L_3 edge can be explained with crystal field theory (§1.6.1). In crystal field theory, high or low spin states can be observed for $3d^4$ – $3d^7$ metal ions depending on the energy difference.[14] Fe^{3+} is usually in a low spin state (strong field) relative to Fe^{2+} ions, hence a higher energy difference between the t_{2g} and e_g states. The ligands also play a role in affecting the multiplet effect as well as the position of the peak. In general, t_{2g} and e_g peak is found to be at 707.3 eV and 708.7 eV respectively (Figure 3.11). A detailed description of the Fe 2p NEXAFS for each of these iron oxide compounds is beyond the scope of this study. Here, the absorption spectra are used to investigate phase changes.

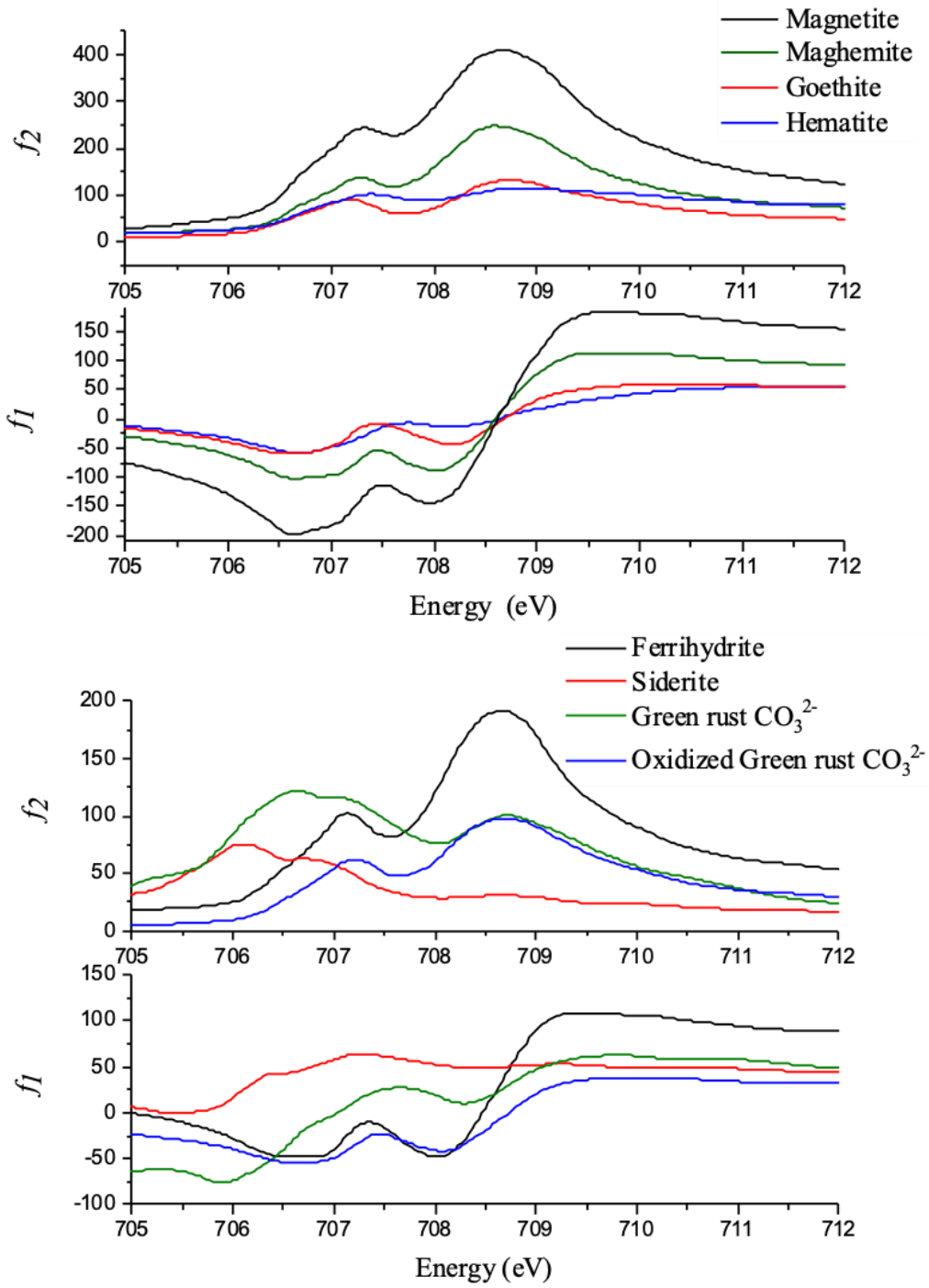

Figure 3.11. Absorption and phase spectra of iron-based compounds (hematite, goethite, maghemite, magnetite, ferrihydrite, siderite, green rust, and oxidized green rust). NEXAFS of iron based compounds obtained from Dr. M. Obst.[40]

Table 3.1. Chemical characteristics of Iron based compounds with NEXAFS data obtained from Dr. M. Obst.[40]

Iron-based compound	Chemical formula	Fe valence	d orbital occupancy
Hematite	$\alpha - Fe_2O_3$	3+	$3d^5\ (t_{2g}{}^3 e_g{}^2)$
Goethite	$FeO(OH)$	3+	$3d^5\ (t_{2g}{}^3 e_g{}^2)$
Maghemite	$\gamma - Fe_2O_3$	3+	$3d^5\ (t_{2g}{}^3 e_g{}^2)$
Magnetite	Fe_3O_4	2+, 3+	$3d^6\ (e_g{}^3 t_{2g}{}^3), 3d^5\ (t_{2g}{}^3 e_g{}^2)$
Ferrihydrite	$(Fe^{3+})_2O_3 \cdot 0.5H_2O$	3+	$3d^5\ (t_{2g}{}^3 e_g{}^2)$
Siderite	$FeCO_3$	2+	$3d^6\ (t_{2g}{}^4 e_g{}^2)$
Green rust/ Oxidized green rust	$[Fe_4^{2+}\ Fe_2^{3+}\ (HO^-)_{12}]^{2+} \cdot [CO_3^{2-} \cdot 2H_2O]^{2-}$	2+, 3+	$3d^6\ (e_g{}^3 t_{2g}{}^3), 3d^5\ (t_{2g}{}^3 e_g{}^2)$

3.6.2 Qualitative observation of the phase spectra

The magnitude of the phase shift in each of the iron compounds corresponds to the magnitude of their optical density except in the case of ferrihydrite (Figure 3.11). For example, magnetite has a distinct absorption band between 707 eV and 709.5 eV, and this is translated in its phase spectra which has the lowest phase signal when compared to the other compounds. This implies that the calculated phase spectra may provide quantitative information however, results here are inconclusive. A much simpler approach to aid in our understanding of the phase spectra will be to perform Kramers-Kronig integral on simple Gaussian functions with the *KK_gui* code[8] and observe the phase change. Kramers-Kronig analysis of a Gaussian function was not performed in this study.

In addition to the results shown above, Kramers-Kronig analysis with *KK_gui* code[8] was performed on the measured absorption spectrum in spectro-ptychography (Figure 3.12 below). All calculated phase spectra were observed to be sensitive below the absorption edge. For instance, magnetite shows a minimum phase signal at 706.6 eV, which is about 1 eV less than its t_{2g} peak in the NEXAFS spectrum. Similarly, in the measured α-Fe_2O_3 ptychography spectrum,

the minimum phase signal lies at 708 eV, which is less than the maximum absorption band at 710 eV. In general, the slope of the phase spectrum corresponds to the absorption edge in a NEXAFS spectrum. This indicates that the phase shift changes significantly at the absorption edge. Therefore, the phase spectra may be a useful tool in the chemical differentiation of closely related species.

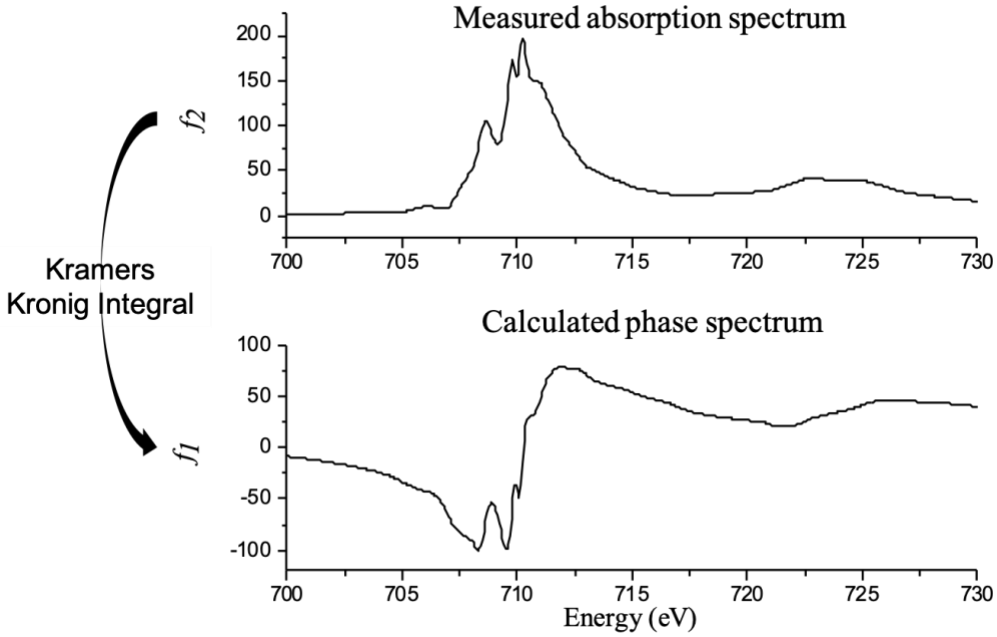

Figure 3.12. Fe 2p NEXAFS spectrum from spectro-ptychography (30 energy points) on Fe_2O_3 is used to estimate the phase spectrum with Kramers-Kronig integral. The integral is calculated with *KK_gui* code.[8]

3.6.3 Comparing measured phase with calculated phase spectra

In this section, the measured phase spectra from ptychography (Figure 3.5) were compared with the calculated phase spectra using Kramers-Kronig transform (Figure 3.12).[8] This is shown together in Figure 3.13, where the spectra in red represent the measured phase and blue represents the calculated phase. Figure 3.13 also shows each phase spectrum at different positions of an iron(III) oxide particle. The measured and calculated phase spectra are similar with a minimum phase signal at 708.5 eV and 710 eV. This suggests that the phase spectrum can be easily reproduced with Kramers-Kronig analysis if it is unable to be extracted from spectro-ptychography measurements. However, there are a few notable differences: the experimental spectra show peak splitting at 710 eV, which is not well-resolved in the calculated spectra. Also, there is a ringing effect observed in the calculated phase spectra from measured absorption at the

edge of the particle (Figure 3.13C). The former observation stated may be due to the smoothing process in the *KK_gui* software[8] used to perform the calculation while the latter is a common issue in signal processing, especially at sharp edges. The sharp edges are a result of the limited energy points acquired in the absorption spectrum used to generate a phase spectrum. Lastly, each of these phase spectra can be compared with the phase spectrum obtained via KK analysis of Dr. M. Obst[40] iron(III) oxide sample (Hematite in Figure 3.11), which is a high-quality NEXAFS spectrum. The author notes that the phase spectrum calculated from Dr. M. Obst[40] NEXAFS spectrum is in good agreement with our phase spectra extracted from the center of the iron(III) oxide particle.

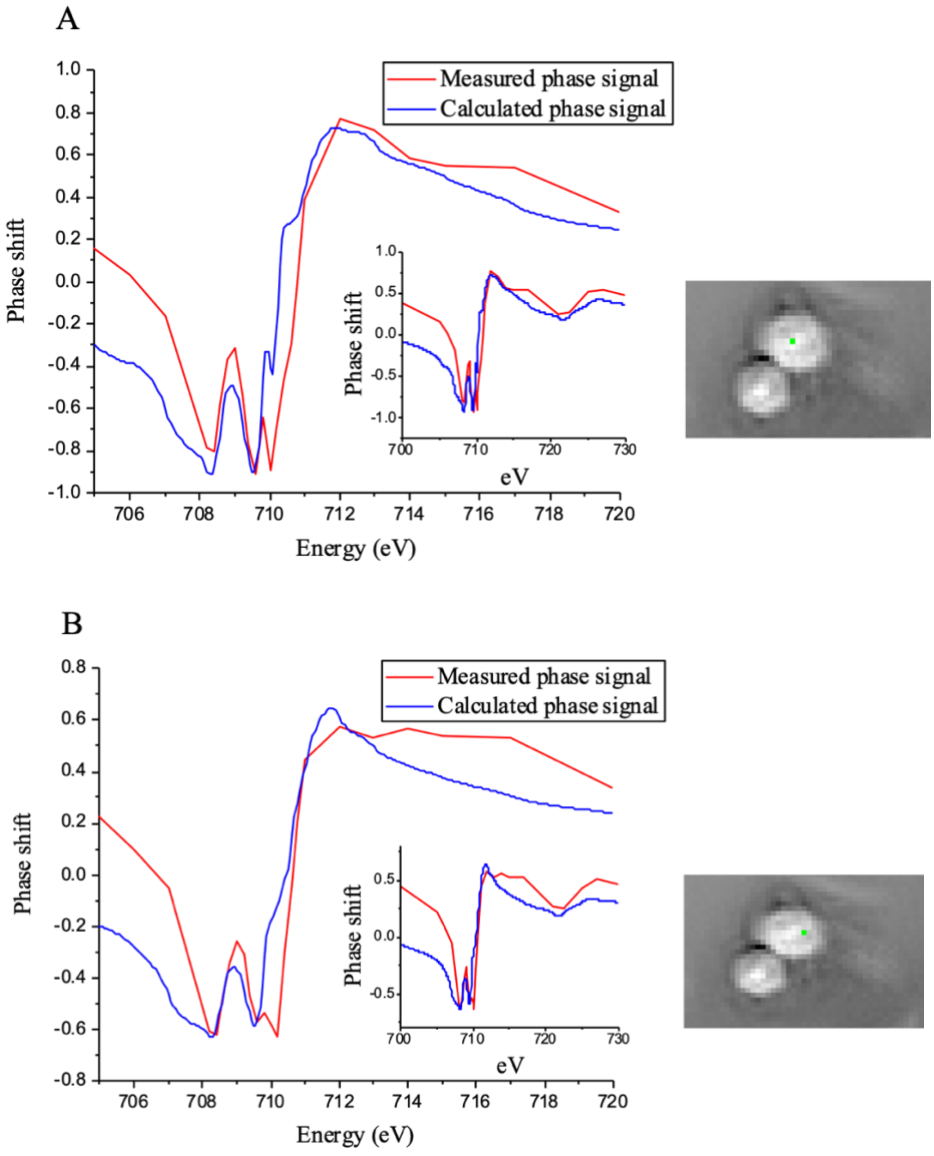

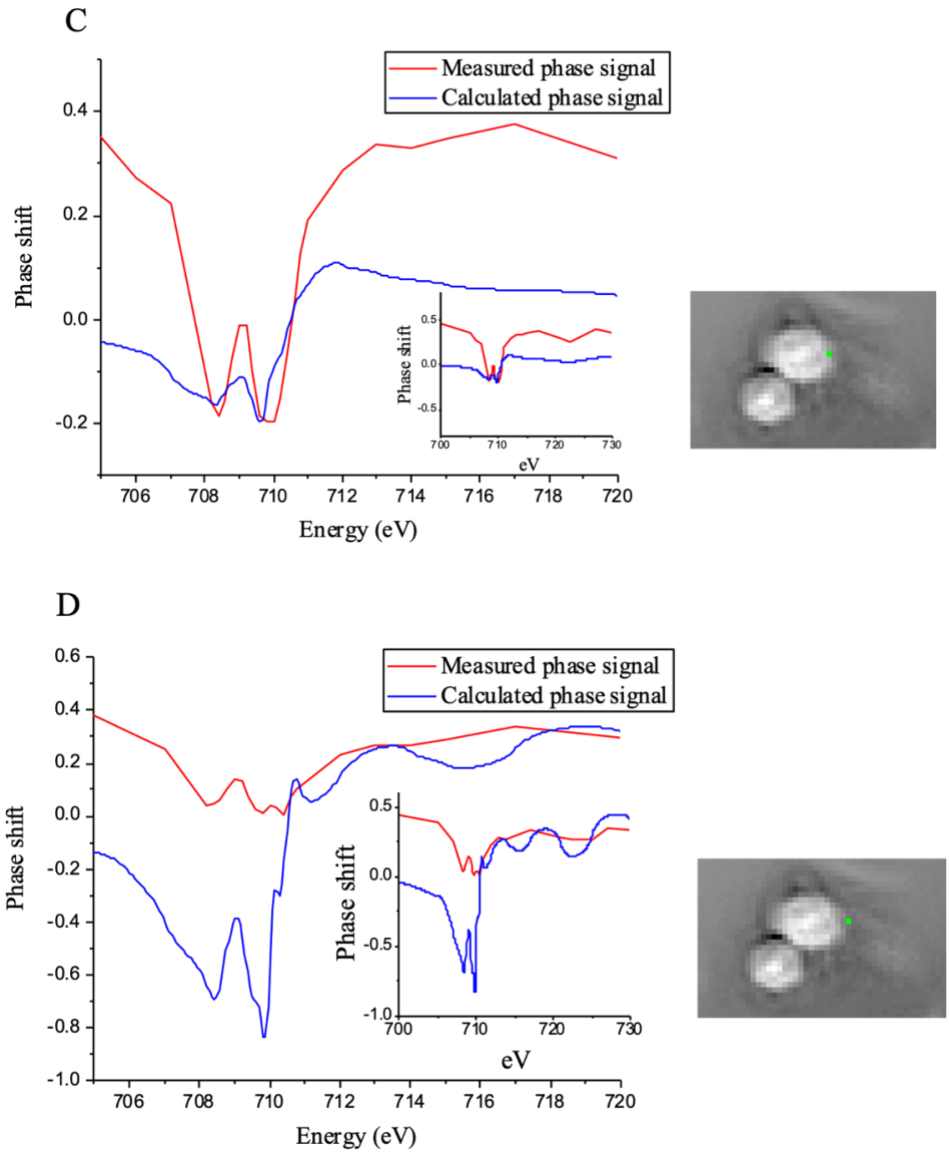

Figure 3.13. Phase spectra from spectro-ptychography experiment (red) and phase spectra calculated using Kramers-Kronig integral[8] (blue) are in good agreement with each other. A – D show spectra extracted from different positions around the Fe_2O_3 nanoparticle. Each calculated phase spectra were obtained using Kramers-Kronig integral on the measured NEXAFS spectro-ptychography data.

CHAPTER 4 DISCUSSION AND CONCLUSION

4.1 Main contributions

This work successfully demonstrates spectro-ptychography at the SM beamline in CLS. Fe_2O_3 nanoparticles were imaged with STXM-ptychography within the Fe $L_{2,3}$ energy range 700 eV – 730 eV. We observed well-resolved images with ptychography method when compared to STXM. Also, the reconstructed images show the expected change in contrast at the absorption edge in Fe $L_{2,3}$ NEXAFS spectra. Spectro-ptychography provides the absorption spectra, which was in good agreement with literature spectra, and a unique phase signal, which is shown to be sensitive to energies below the absorption edge. The phase signal changes more significantly than the absorption signal at the absorption edge. Therefore, the phase may be advantageous for chemical differentiation around the absorption resonance.[33]

This work also explores areas surrounding a particle to evaluate how the spectra changes with position. Results show that there was no observable difference in chemistry but rather in the amount of material present. This test is useful to obtain chemical maps for a region around a single particle. Since NEXAFS is sensitive to the oxidation state, one can differentiate between different oxidation states of iron present in the sample. Spectro-ptychography maps based on NEXAFS has been shown to be useful in elucidating the degradation of Li-rich cathodes, where the oxidation state for each component that make up the cathode can be visualized.[44]

4.2 Summary of the challenges with performing ptychography at CLS

Our ability to find a suitable sample area with STXM remains an issue that needs to be addressed. The goal to look at monodispersed 15 nm – 20 nm iron oxide nanoparticles is impacted by this issue. Although these nanoparticles were visible with TEM, we were limited by STXM's ability to show well-defined monodispersed particles at such a small scale. Recall that the spatial resolution of STXM is typically around 30 nm.[1,2] This means that there is an uncertainty associated with performing ptychography on smaller-sized nanoparticles as they are too small to see with STXM. There are two possible solutions to this problem: First, look for something bigger in the same focal plane to help focus on smaller particles. A second solution will be to focus and navigate in ptychography mode. The later solution requires fast real-time processing of the data to be feasible. Figure 4.1 illustrates how to make ptychography

experiments work reliably by having in place a live view of the ongoing reconstruction. As data is collected, the diffraction images from a ptychography scan are immediately transferred to a dedicated ptychography computer with the pyPIE software[44], which is a significant improvement on the previously used SHARP code for data processing. The pyPIE software supports energy range definition useful to process ptychography diffraction images measured at a sequence of energies. It also provides the amplitude and phase images as a function of the number of iterations in the phase retrieval process. The amplitude and phase images can be used to navigate around other interesting regions or zoom into a region of interest thus allowing familiar microscopic functionality. §4.5 will discuss long-term goals in processing ptychographic data.

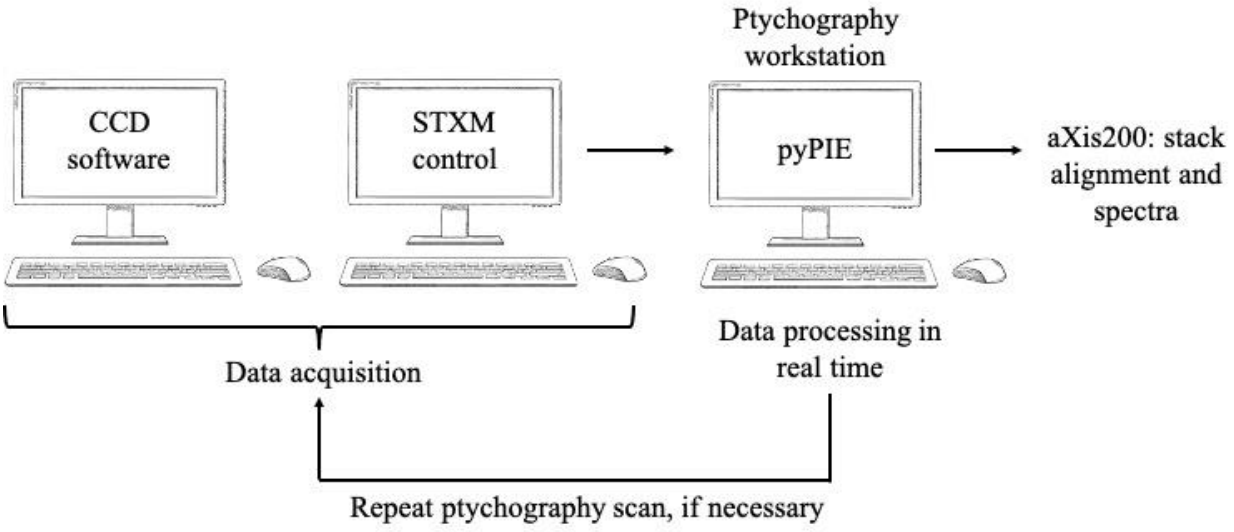

Figure 4.1. Ptychography data flow from data acquisition to data processing in real time. Image stack alignment and spectra (spectro-ptychography) can be performed offline.

This work also identifies other challenges in data acquisition and image processing with SHARP. Mechanical instabilities and vibrations can play a role in affecting the quality of data (§3.5.3) and there is a risk of obtaining significant artifacts during image processing (§3.5.6). Recent work not discussed in this thesis has been performed to optimize spectro-ptychography data acquisition in defocus mode by imaging a large field of view, and processing images of the sample with pyPIE.

4.3 Amplitude and phase information

As mentioned in previous chapters, the amplitude and phase information obtained complement each other. In Figure 3.4, the phase images show a higher change in contrast relative to amplitude (intensity) images. In fact, we can observe well-defined nanoparticles with internal structures as shown in Figure 4.2. These fine structures within the nanoparticle aggregate are not visible in an intensity image. Rodenburg[28] states that the intensity information in the Fourier domain is less important than the phase in resolving the structure of an object. The intensity image describes the attenuation of a wave as it interacts with the object, while the phase of a wave encodes most of the structural information within it.[28] Therefore, the phase information is sensitive to fine details in a sample, especially where nanoparticles are aggregated or stacked upon each other. The sensitivity of the phase information in spectro-ptychography has also been observed in other studies.[33-35] The benefit of spectro-ptychography is that the amplitude can be effective for quantitative analysis and the phase can be used to improve image contrast in spectro-microscopy.

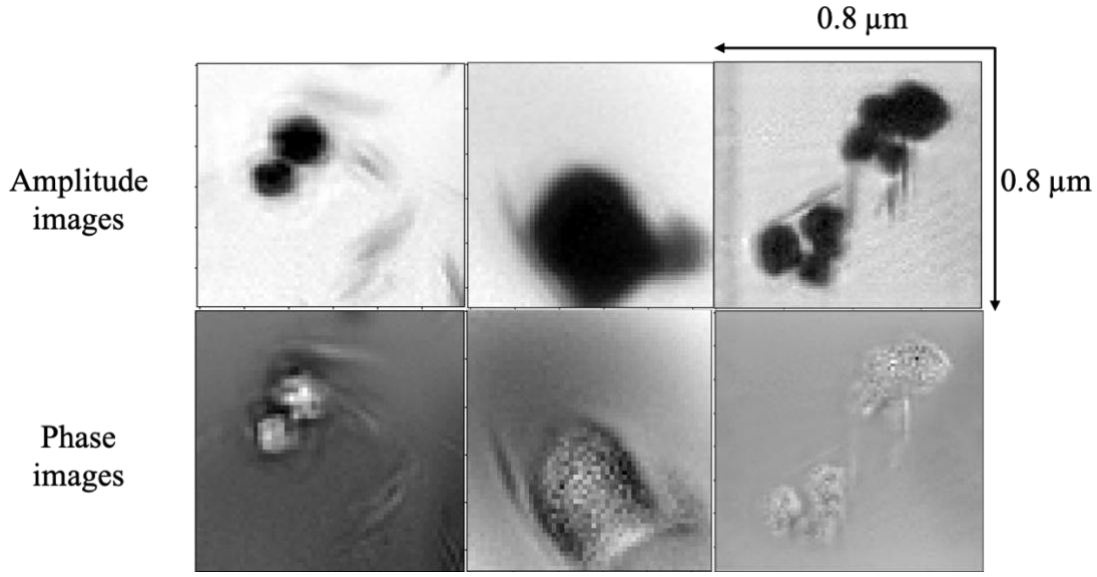

Figure 4.2. Ptychography amplitude and phase images acquired at 710 eV. The phase images are sensitive to fine details in the sample that are not visible in an amplitude image.

There are other phase-contrast imaging techniques that exist to take advantage of the highly sensitive phase information. Particularly in radiology, where X-rays are intended to penetrate biological materials for medical diagnosis. In such a case, the absorption contrast between different parts of an object in radiological images is usually weak especially when

materials with similar absorption cross-sections are investigated (e.g., in mammography).[52,53] On the other hand, phase images are more sensitive to weakly absorbing materials and can be used to improve image contrast. The reason for this is because absorption, β typically decreases with the fourth power of the photon energy while the phase contrast, δ scales with the inverse square of the energy.[51,54] In this work, we note that the minimum signal in phase spectra is sensitive below the absorption edge of iron(III) oxide (Figure 3.5). Also. the measured phase is inherently quantitative[54] as shown in Figure 3.7, where phase spectra were obtained at regions around a particle. The following section discusses the use of Kramers-Kronig relations to explore whether phase spectra is reliable for quantitative analysis.

4.4 Use of Kramers-Kronig relation

Kramers-Kronig analysis re-emphasizes the sensitivity of the phase signal and its potential to discriminate between samples with similar absorption peaks. However, results regarding the quantitative nature of the phase spectra are inconclusive. Results show that the calculated phase spectra obtained from normalized Fe 2p NEXAFS spectra may be used to estimate the relative quantity of measured samples. As mentioned in chapter 1, the phase can be related to the thickness of a sample as $exp[ik\delta z]$ similar to intensity attenuation, $exp[-2k\beta z]$ (Equation 1.14 and 1.15).[8] See supplementary information for detailed equations. Since this is a complex number, the phase spectrum itself may not directly infer that it can be used for quantitative analysis. The author of this work proposes that intensity changes may be measured from the steepness of the slope in phase signal. For example, a very steep slope as in the case of magnetite in Figure 3.11, estimates the relative intensity. This idea remains unclear and further tests on a simple Gaussian function may help visualize how the phase spectra changes with the intensity.

To summarize, this work shows the importance of phase spectra in analyzing weak or similar absorbing species, and their sensitivity to energies below the absorption edge. This work also demonstrates the conversion of absorption spectra to phase spectra. Although this is not a new method, Kramers-Kronig transform remains a relevant tool to use in spectra analysis.[8,36] Measured phase spectra from ptychography and Kramers-Kronig calculated phase spectra are in good agreement with each other. The author concludes that the use of phase spectra for chemical analysis requires further exploration.

4.5 Moving forward

4.5.1 A fast data acquisition process

A few improvements can be made to realize the broad goal of imaging smaller nanoparticles and to identify the analytical limits of ptychography. One of the improvements that can be made involves the type of CCD detector used for image capture. A CCD with more pixels and a high dynamic range will be more effective in capturing the high-frequency component in the diffraction pattern. This can result in a higher resolution image. We also note that a fly-scan approach, which reduces the detector read-out time, will become more important as brighter X-ray sources are developed.[47] Decreasing the CCD dead time is necessary for a more efficient data acquisition process, albeit at the expense of an increase in computational cost. The increased computational cost in the fly-scan or continuous scan method is due to its reconstruction method and sensitivity to noise when compared to step scan ptychography.[55] However, technological advances in computational software and hardware are expected to minimize the computational cost.

4.5.2 A fast and robust algorithm for data processing

Faster algorithms are necessary for large amounts of spectro-ptychography data. Future directions in dealing with such large amounts of data involve parallel computing, where many processes can be carried out simultaneously. A recent development on a generic image reconstruction framework called Adorym, written for parallel processing of ptychographic data has the potential to improve reconstructed image quality.[56] This framework is interesting because it optimizes the object function $T(r)$ and refines other experimental parameters e.g. the probe position, to address practical issues encountered in experiments.[56] It can be applied to other related imaging techniques (§4.5.3) that rely on a phase retrieval process to reconstruct an image. Lastly, it can be extended to other phase retrieval algorithms not discussed in this thesis such as Hybrid input-output (HIO),[43,57] and difference map.[58]

4.5.3 More functional for a wide range of samples

Other related techniques can be used depending on the scientific purpose of the study. For example, ptychography can be combined with conventional methods like tomography referred to as ptycho-tomography. Ptycho-tomography exploits the high-resolution coherent

diffraction imaging in ptychography to obtain true 3D information on samples.[54] Also, the phase projections measured at different sample orientations can be tomographically combined to obtain a 3D map of the sample's refractive index proportional to its electron density distribution.[59] Spectroscopic information can also be obtained by repeating such measurement at a sequence of energies (spectro-ptycho-tomography).[60,61]

Ptycho-tomography is typically used in biomedical research applications and most cases, these biological samples easily undergo radiation damage. In such cases, radiation-sensitive or wet biological samples can be studied at cryogenic temperatures without the need for sample preparation steps that may induce artifacts in measurements.[62] The techniques described here will ensure that a wide range of samples can be measured. Since these techniques are closely related, a multi-modal end station at the SM beamline, CLS is preferred to enable such experiments with ease. The setup to perform a cryo-spectro-ptycho-tomography experiment requires a goniometer allowing for sample rotation, a cryo-holder for a low-temperature environment, an ultra-high vacuum at about 10^{-8} torr, and a high-speed CCD camera.

As mentioned in chapter 1, one of the advantages of ptychography is its ability to image non-periodic samples with unlimited size. This is because any image, regardless of the size of its field of view, can always be represented computationally as one big unit cell.[28] The iron(III) oxide NP's used here are not crystalline and as expected the intensity of the diffraction between regions in a particle is weak (Figure 3.3). An interesting study could involve the relationship between the crystalline order in samples and the image quality provided by ptychography. A good start is to record images of bigger and more crystalline samples in a quest to explore this with ptychography.

4.5.4 The next generation of light source

Incident and coherent brilliant X-rays from 4th generation synchrotron sources (e.g., Free Electron Lasers for soft X-ray radiation) are expected to further broaden the range of application for ptychography. For example, imaging with ultrashort femtosecond pulses will enable the study of time-resolved processes at a high spatial resolution. Also, the increased coherence in 4th generation synchrotron facilities can play a role in increasing the intensity in the diffraction image and improving the resolution of the reconstructed image.[63] Other experimental factors that affect ptychography data set are the CCD detector efficiency and dynamic range.[28] Data

acquisition and data processing will need to be effective to benefit from the enhanced performance of a new generation light source.

Aside from imaging, one of the properties of ptychography (or any phase retrieval method) is its ability to be used to characterize an X-ray beam.[64] Ptychography can be used in beam diagnostics because it provides the complex wavefront of the incident illumination, $P(r, E)$ as a by-product.[64,65] Partially coherent probes can be reconstructed along with the complex transmission function $T(r)$.[63] Analysis of the reconstructed probe can be useful in characterizing beam quality but there are currently few studies that have explored ptychography for this purpose. With the advent of 4th generation light source and technological advancements in ptychography data acquisition and processing, ptychography has the potential to be a conventional spectro-microscopy technique.

CHAPTER 5 SUPPLEMENTARY INFORMATION

5.1 The SM beamline control

Chapter 2 provides an overview of the operation of the STXM microscope using the SM beamline control computer. Measurements were performed between 710 ev and 730 eV using circularly left polarization.

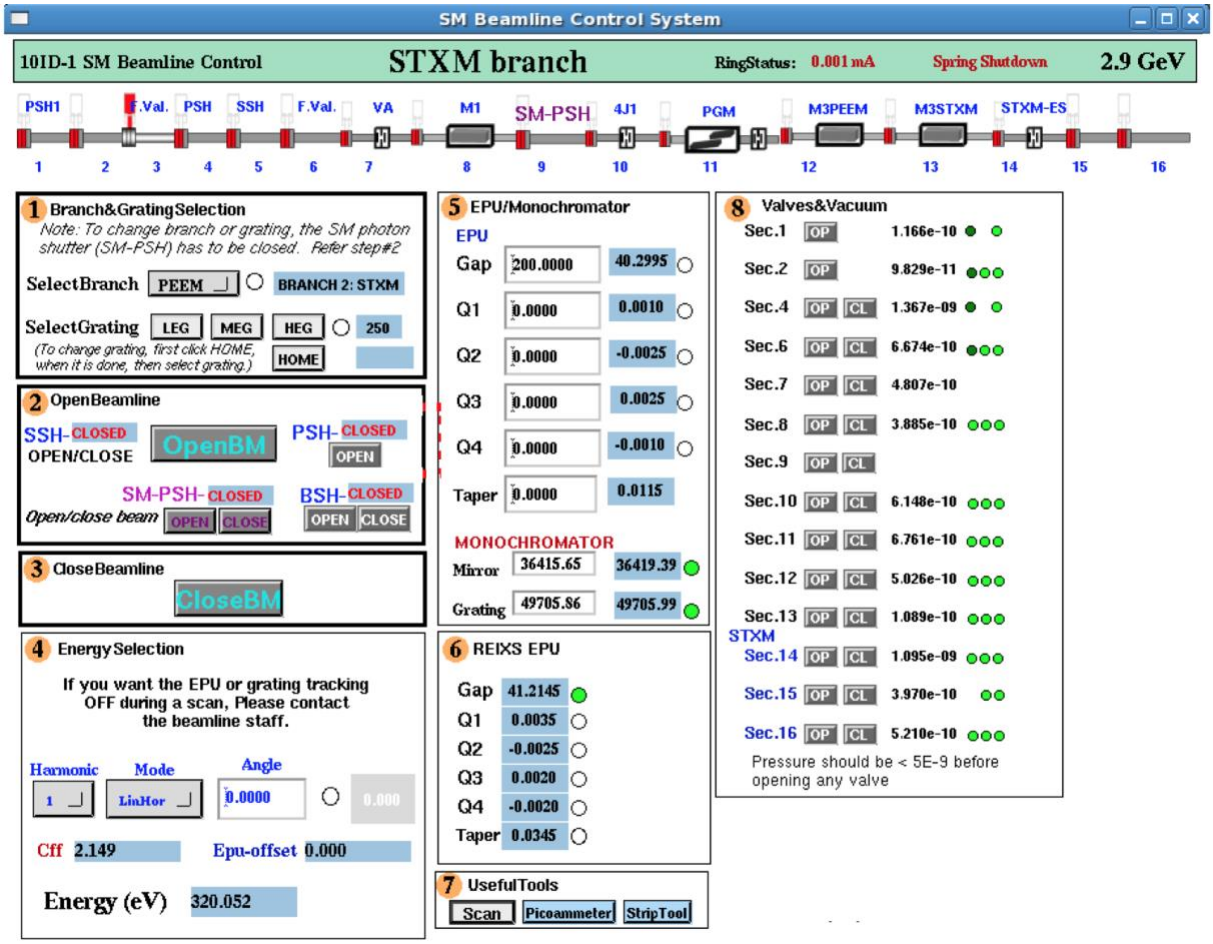

Figure 5.1. STXM branch GUI on the SM beamline control computer. This is used to control components in the beamline including the shutters, EPU, grating, mirrors and more. Figure obtained from CLS SM beamline manual.[66]

5.2 Spectro-ptychography images

5.2.1 Amplitude and phase images at 30 energy points

The following images show the amplitude and phase at each energy point. Observe the change in contrast from 700 eV to 730 eV. The highest contrast amplitude and phase image is at 711 eV and 710.2 eV respectively.

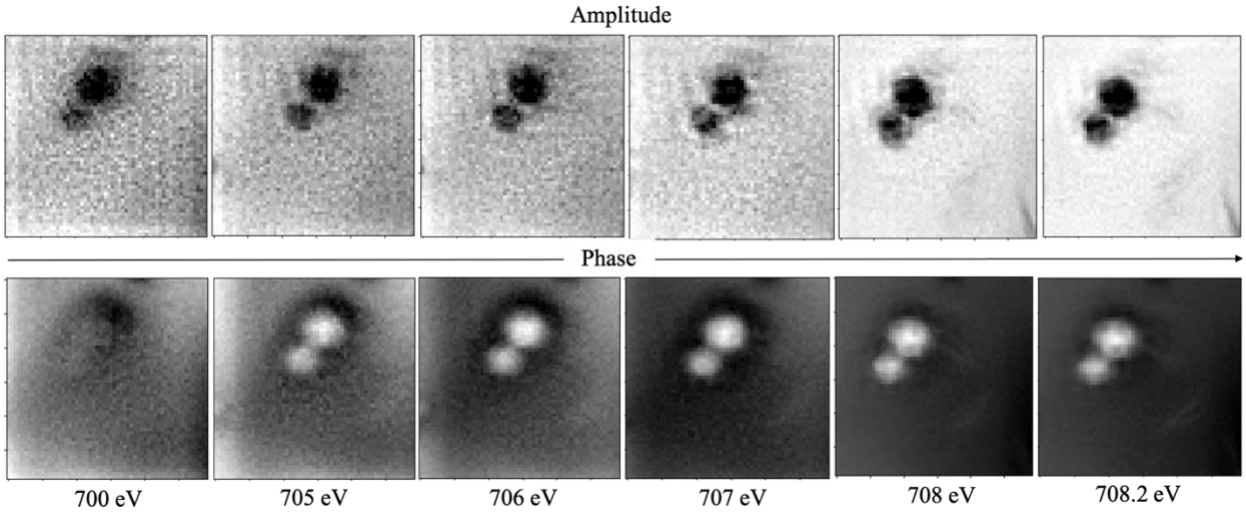
Amplitude
Phase
700 eV
705 eV
706 eV
707 eV
708 eV
708.2 eV

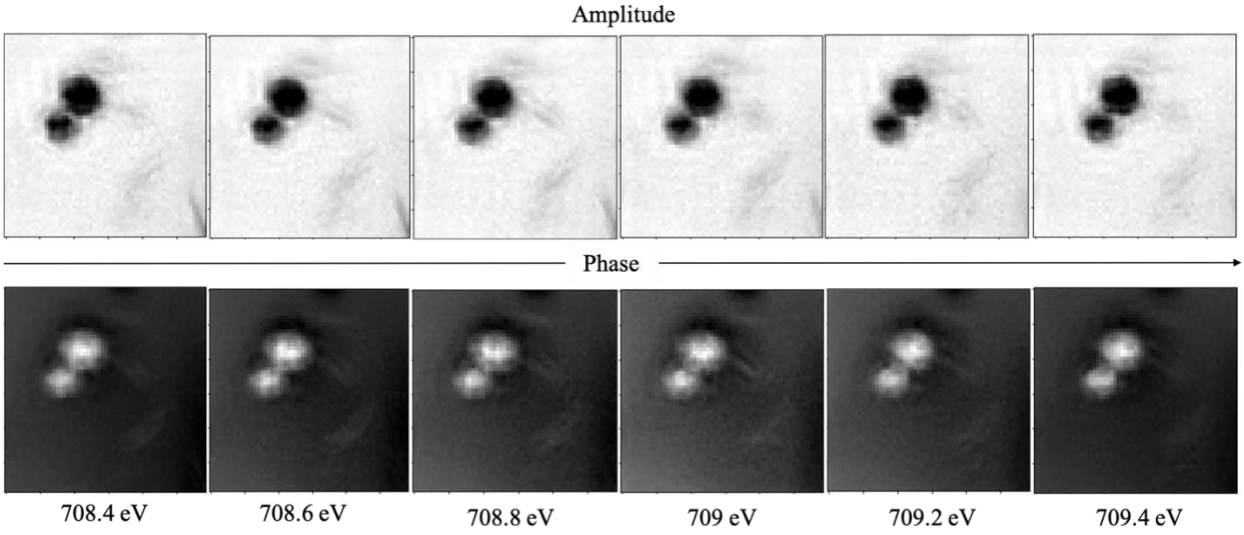
Amplitude
Phase
708.4 eV
708.6 eV
708.8 eV
709 eV
709.2 eV
709.4 eV

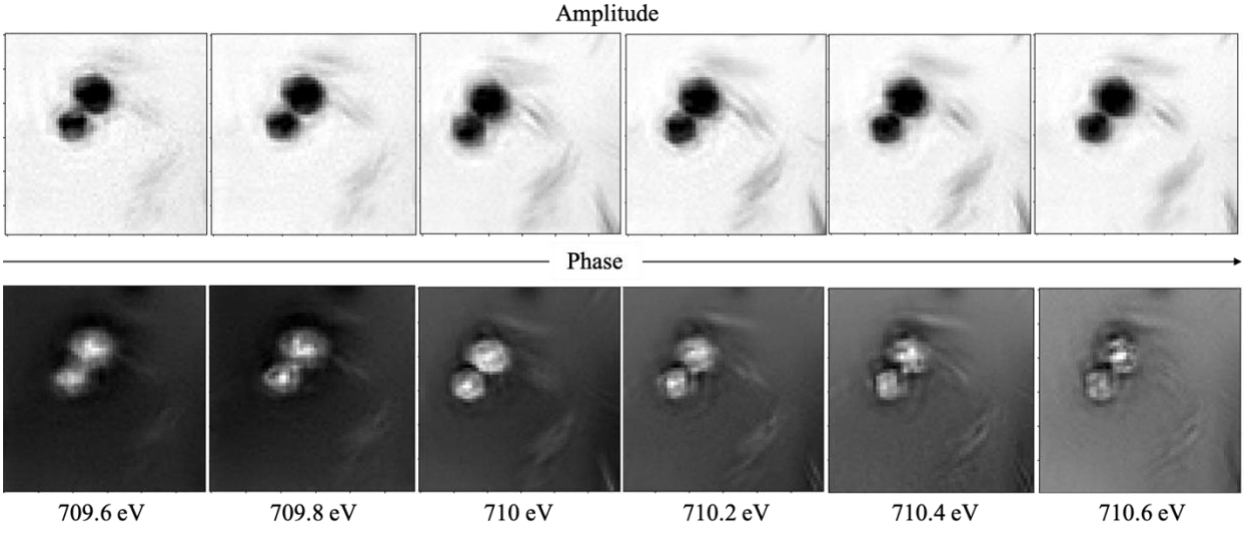
Amplitude
Phase
709.6 eV
709.8 eV
710 eV
710.2 eV
710.4 eV
710.6 eV

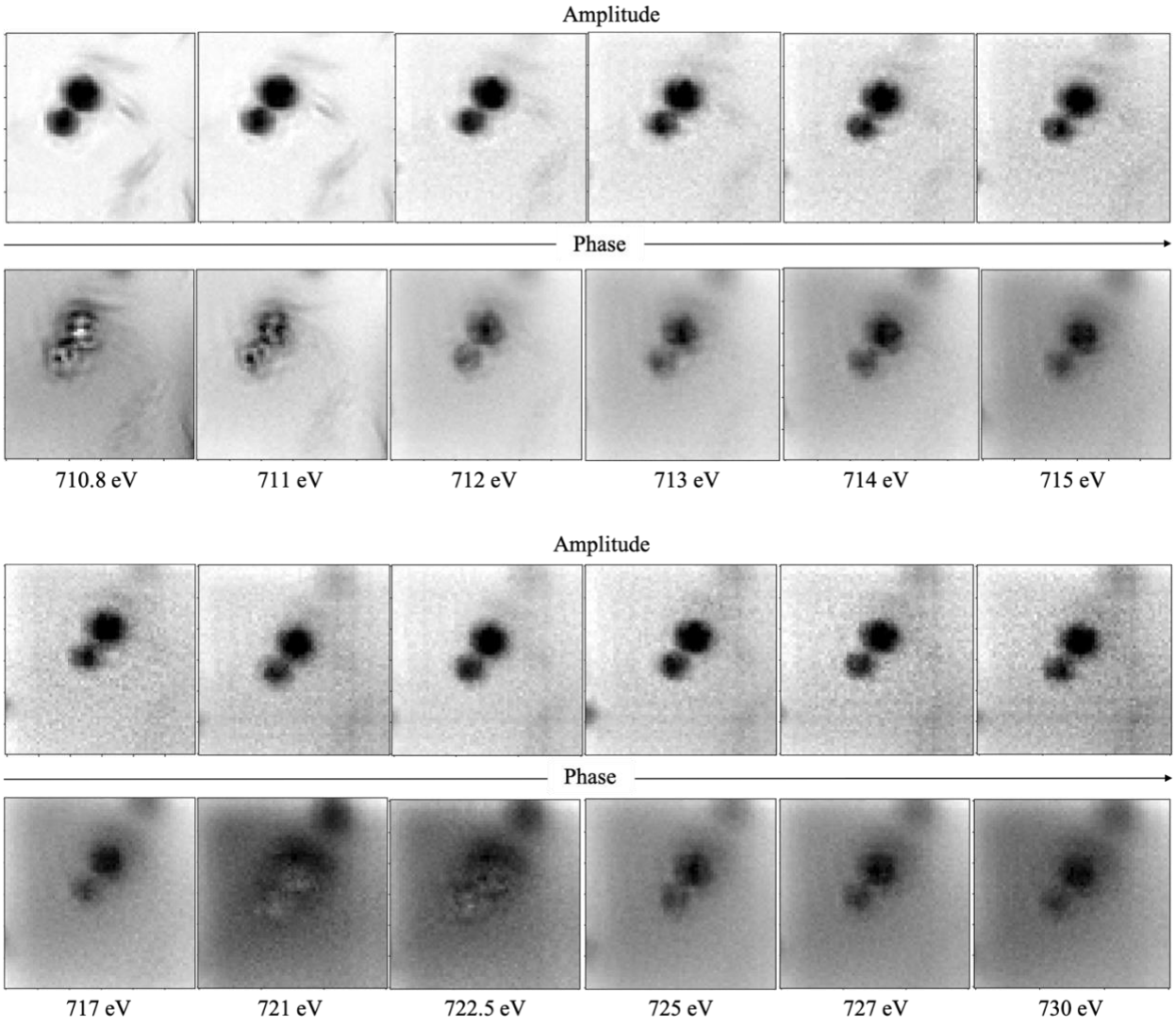

Figure 5.2. Amplitude and phase images at each energy point measured. These images were used to obtain the spectra shown in Figure 3.5.

5.3 STXM microscope parameters

5.3.1 7 energy points

STXM-ptychography microscope parameters for a fine scan F and ptychography scan Pt.

Scan number	Type of scan	Scan size (x, y) in µm	Pixel number (x, y)	Energy (eV)	Dwell time in ms	Exit slits (Dispersive/ Nondispersive)	EPU	Pitch
190612-038	F	10 x 10	150 x 150	700	1	10/ 10	-0.7	-14.8

190612-044	Pt	0.8 x 0.8	16 x 16	700	2300	10/ 10	-0.7	-14.8
190612-045	Pt	0.8 x 0.8	16 x 16	708	2300	10/ 10	-0.7	-14.8
190612-046	Pt	0.8 x 0.8	16 x 16	711	2300	10/ 10	-0.7	-14.8
190612-047	Pt	0.8 x 0.8	16 x 16	709	2300	10/ 10	-0.7	-14.8
190612-048	Pt	0.8 x 0.8	16 x 16	707	2300	10/ 10	-0.7	-14.8
190612-049	Pt	0.8 x 0.8	16 x 16	712	2300	10/ 10	-0.7	-14.8
190612-050	Pt	0.8 x 0.8	16 x 16	710	2300	17/ 17*	-0.7	-14.8

Table 5.1. Parameters used for STXM-ptychography scans shown in Figure 3.4. The 7 energy points are listed according to their scan numbers. * A wider slit size was used to increase the flux.

5.3.2 30 energy points

Scan number	Type of scan	Scan size (x, y) in µm	Pixel number (x, y)	Energy (eV)	Dwell time in ms	Exit slits (Dispersive/ Nondispersive)	EPU	Pitch
200802-000	F	5 x 5	150 x 150	710	2	15/ 15	-1.3	-8.3
190612-001-030	Pt	0.8 x 0.8	16 x 16	700 - 730	2300	15/ 15	-0.7	-14.8

Table 5.2. Parameters used for STXM-ptychography scans shown in Figure 3.5.

5.4 Kramers-Kronig Relations

All relevant equations discussed in this thesis are outlined here for reference.

Complex valued image of object and probe

$$\psi_{(r)}^{j} = T(r,E) \cdot P(r,E) \quad 5.1$$

According to Beer's Law $A = \varepsilon cl$ however, absorbance does not always measure absorption but attenuated light. Attenuation depends on absorption, reflection, light scattering, and other physical processes. In this section we will use a closely related quantity referred to as optical depth (OD).

$$OD = \mu\rho t = -ln\frac{I}{I_0} = -\ln T \quad 5.2$$

Where μ is the mass absorption coefficient, ρ is the density, and t is thickness of material. The multiplicative complex transmission function includes the modulus and phase….

$$T(r,E) = exp\,(2\pi i(n(r,E)-1)\,t(r)/\lambda) \quad 5.3$$

Where *n(r, E)* is the complex refractive index, *t(r)* is the local sample thickness, and λ is wavelength.

$$n(r,E) = 1 - \delta(r,E) + i\beta(r,E) \quad 5.4$$

δ and β are expressed as the real and imaginary part of the anomalous term of the atomic scattering factors f_1 and f_2.

$$n(r,E) = 1 - \delta(r,E) + i\beta(r,E) = 1 - K(f_1 + if_2) \quad 5.5$$

$$K = \frac{n_a r_e \lambda^2}{2\pi} \quad 5.6$$

From equation we can express δ and β as

$$\delta = \frac{r_e\lambda^2}{2\pi} n_a f_1 \quad 5.7$$

$$\beta = \frac{r_e\lambda^2}{2\pi} n_a f_2 \quad 5.8$$

The intensity attenuation $exp[-2k\beta z]$ and phase advance $exp[ik\delta z]$ can be written in terms of a frequency dependent complex number of atoms per electron $(f_1 + if_2)$.[8]

f_2 Values are obtained from X-ray absorption data: $I_{fluorescence} \propto {-dI}/{dz} = 2k\beta = 2n_a r_e \lambda f_2$

We can relate the real and imaginary parts using Kramers-Kronig Relations.

$$f_1(\omega) = 1 + \frac{2}{\pi} P \int_0^\infty \frac{\omega' f_2(\omega')}{\omega'^2 - \omega^2} d\omega' \quad 5.9$$

$$f_2(\omega) = -\frac{2\omega}{\pi} P \int_0^\infty \frac{f_1(\omega' - 1)}{\omega'^2 - \omega^2} d\omega' \quad 5.10$$

Where P is the principal part of a complex integral and ω is the complex variable as it approaches infinity. The equation can be simplified in terms of f_1, f_2 spectrum, and the integration photon energy, ϵ to give

$$f_1(E) = Z + \frac{2}{\pi}\int_0^{\infty} \frac{\epsilon\, f_2(\epsilon)}{E^2 - \epsilon^2} d\epsilon - \Delta f_r \qquad 5.11$$

$$f_1(E) = Z + \frac{2}{\pi}\int_0^{\infty} \kappa f_2(\epsilon)\, d\epsilon - \Delta f_r \qquad 5.12$$

$E = {}^{hc}/_{\lambda}$ Is the determination photon energy, Δf_r is the relativistic correction term – negligible for soft X-rays, and κ is the energy dependent weighting of $f_2(\epsilon)$ data.

5.5 Dynamic Light Scattering

In dynamic light scattering, particles are characterized based on how they interact with light. This result provides dynamic information of the particles in solution via autocorrelation function. Size of NP aggregates are greater than 150 nm.

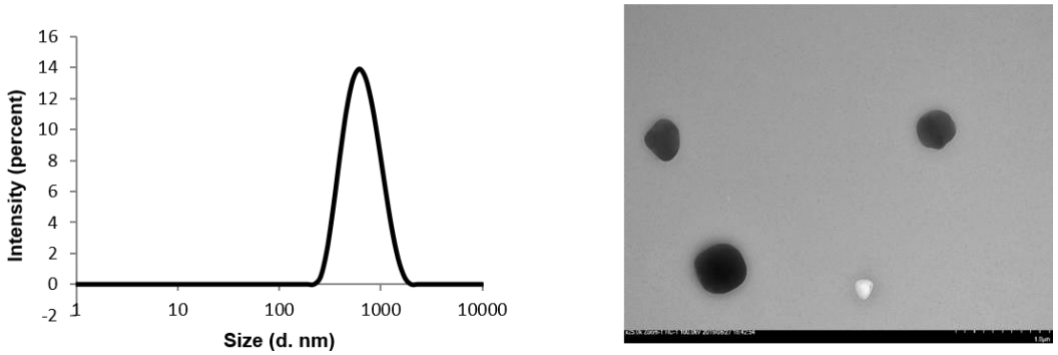

Figure 5.3. Left. Overview on the size distribution of Fe_2O_3 nanoparticles. Result shows iron(III) oxide NP's form aggregate structures. Right. TEM image.

References

1. Hitchcock, A. P. Soft X-ray Spectromicroscopy and Ptychography. *Journal of Electron Spectroscopy and Related Phenomena*. **2015,** *200*, 49-63.
2. Ade, H.; Hitchcock, A. P. NEXAFS Microscopy and Resonant Scattering: Composition and Orientation Probed in Real and Reciprocal Space. *Polymer*. **2008,** *49* (3), 643-675.
3. Karunakaran, C.; Christensen, C. R.; Gaillard, C.; Lahlali, R.; Blair, L. M.; Perumal, V.; Miller, S. S.; Hitchcock, A. P. Introduction of Soft X-ray Spectromicroscopy As an Advanced Technique for Plant Biopolymers Research. *Public Library of Science One.* **2015,** *10* (3), 1-18.
4. Als-Nielsen, J.; McMorrow, D. Chapter 1 X-rays and Their Interaction With Matter. *Elements of Modern X-ray Physics*. Second Edition; John Wiley & Sons: United Kingdom, **2011**.
5. Stöhr, J. Chapter 4 Experimental and Calculated K-shell Spectra of Simple Free Molecules. *NEXAFS Spectroscopy*. First Edition; Springer: Berlin, **1996;** Vol. 25.
6. Atwood, D., *Soft X-rays and Extreme Ultraviolet Radiation. Principles and Applications.* First Edition; Cambridge University Press: New York, **1999**.
7. Henke, B. L.; Gullikson, E. M.; Davis, J. C. X-ray Interactions: Photoabsorption, Scattering, Transmission and Reflection E= 50-30,000 ev, Z= 1-92. *Atomic Data and Nuclear Data Tables.* **1993,** *54* (2), 181-342.
8. Jacobsen, C. J.; Wang, S. Y.; Yun, W.; Frigo, S. Calculation of X-ray Refraction from Near-Edge Absorption Data Only. *SPIE, Optical Constants of Materials for UV to X-ray Wavelengths*. **2004,** *5538*, 23-30.
9. Urquhart, S.; Ade, H. Chapter 6 NEXAFS Spectroscopy and Microscopy of Natural and Synthetic Polymers. *Chemical Applications of Synchrotron Radiation;* Sham, T. Ed.; World Scientific Publishing: Singapore, **2002;** Vol 12A, *285*.
10. De Groot, F. Multiplet Effects in X-ray Spectroscopy. *Coordination Chemistry Reviews* **2005,** *249* (1-2), 31-63.
11. Urquhart, S. G. Delocalization and Functional Group Fingerprinting in The Core Excitation Spectroscopy of Molecules and Polymers. Ph.D. Thesis, McMaster University, **1997**.
12. De Groot, F.; Kotani, A. Chapter 6 X-ray Absorption Spectroscopy. *Core Level Spectroscopy of Solids*. CRC Press: Boca Raton, **2008**.

13. Bethe, H. A. *Splitting of Terms in Crystals: Complete English Translation*. Consultants Bureau: **1929;** Vol. 3.

14. Miedema, P. S.; De Groot, F. M. The Iron L edges: Fe 2p X-ray Absorption and Electron Energy Loss Spectroscopy. *Journal of Electron Spectroscopy and Related Phenomena*. **2013,** *187*, 32-48.

15. Yoon, T. H. Applications of Soft X-ray Spectromicroscopy in Material and Environmental Sciences. *Applied Spectroscopy Reviews*. **2009,** *44* (2), 91-122.

16. Park, T.-J.; Sambasivan, S.; Fischer, D. A.; Yoon, W.-S.; Misewich, J. A.; Wong, S. S. Electronic Structure and Chemistry of Iron-Based Metal Oxide Nanostructured Materials: A NEXAFS Investigation of $BiFeO_3$, $Bi_2Fe_4O_9$, α-Fe_2O_3, γ-Fe_2O_3, and Fe/Fe_3O_4. *The Journal of Physical Chemistry C.* **2008,** *112* (28), 10359-10369.

17. Kelly, K. L.; Coronado, E.; Zhao, L. L.; Schatz, G. C. The Optical Properties of Metal Nanoparticles: The Influence of Size, Shape, and Dielectric Environment. *Journal of Physical Chemistry B.* **2003,** *107* (3), 668-677.

18. Sun, S.; Zeng, H.; Robinson, D. B.; Raoux, S.; Rice, P. M.; Wang, S. X.; Li, G. Monodisperse MFe_2O_4 (M= Fe, Co, Mn) Nanoparticles. *Journal of the American Chemical Society.* **2004,** *126* (1), 273-279.

19. Song, Y.; Zhang, Z.; Elsayed-Ali, H. E.; Wang, H.; Henry, L. L.; Wang, Q.; Zou, S.; Zhang, T. Identification of Single Nanoparticles. *Nanoscale.* **2011,** *3* (1), 31-44.

20. Crocombette, J.; Pollak, M.; Jollet, F.; Thromat, N.; Gautier-Soyer, M. X-ray Absorption Spectroscopy at The Fe $L_{2,3}$ Threshold in Iron Oxides. *Physical Review B.* **1995,** *52* (5), 3143.

21. Anderson, E. H.; Olynick, D. L.; Harteneck, B.; Veklerov, E.; Denbeaux, G.; Chao, W.; Lucero, A.; Johnson, L.; Attwood, D. Nanofabrication and Diffractive Optics for High-Resolution X-ray Applications. *Journal of Vacuum Science & Technology B: Microelectronics and Nanometer Structures Processing, Measurement, and Phenomena*. **2000,** *18* (6), 2970-2975.

22. Lam, K. P.; Hitchcock, A. P.; Obst, M.; Lawrence, J. R.; Swerhone, G. D.; Leppard, G. G.; Tyliszczak, T.; Karunakaran, C.; Wang, J.; Kaznatcheev, K. Characterizing Magnetism of Individual Magnetosomes by X-ray Magnetic Circular Dichroism in A Scanning Transmission X-ray Microscope. *Chemical Geology.* **2010,** *270* (1-4), 110-116.

23. Jacobsen, C.; Wirick, S.; Flynn, G.; Zimba, C. Soft X-ray Spectroscopy From Image Sequences with Sub-100 nm Spatial Resolution. *Journal of Microscopy.* **2000,** *197* (2), 173-184.

24. Guttmann, P.; Rehbein, S.; Werner, S.; Henzler, K.; Tarek, B.; Schneider, G. Nanoscale Spectroscopy and Tomography with The HZB X-ray Microscope: Applications in Materials and Life Sciences. *Journal of Physics: Conference Series.* **2013,** *463,* 012032.

25. Thibault, P.; Guizar-Sicairos, M.; Menzel, A. Coherent Imaging at the Diffraction Limit. *Journal of Synchrotron Radiation.* **2014,** *21* (5), 1011-1018.

26. Giewekemeyer, K.; Beckers, M.; Gorniak, T.; Grunze, M.; Salditt, T.; Rosenhahn, A. Ptychographic Coherent X-ray Diffractive Imaging in the Water Window. *Optics Express.* **2011,** *19* (2), 1037-50.

27. Miao, J.; Ishikawa, T.; Shen, Q.; Earnest, T. Extending X-ray Crystallography to Allow the Imaging of Noncrystalline Materials, Cells, and Single Protein Complexes. *Annual Review of Physical Chemistry.* **2008,** *59,* 387-410.

28. Rodenburg, J. M., Ptychography and Related Diffractive Imaging Methods. *Advances in Imaging and Electron Physics.* **2008,** *150,* 87-184.

29. Hoppe, W., Diffraction in Inhomogeneous Primary Wave Fields. Amplitude and Phase Determination For Nonperiodic Objects. *Acta Crystallographica Section A.* **1969**, 508.

30. Hirose, M.; Shimomura, K.; Burdet, N.; Takahashi, Y. Use of Kramers–Kronig Relation in Phase Retrieval Calculation in X-ray Spectro-ptychography. *Optics Express.* **2017,** *25* (8), 8593-8603.

31. Pfeiffer, F., X-ray ptychography. *Nature Photonics.* **2018,** *12* (1), 9-17.

32. Marchesini, S.; Krishnan, H.; Daurer, B. J.; Shapiro, D. A.; Perciano, T.; Sethian, J. A.; Maia, F. R. SHARP: A Distributed GPU-Based Ptychographic Solver. *Journal of Applied Crystallography.* **2016,** *49* (4), 1245-1252.

33. Zhu, X.; Hitchcock, A. P.; Bazylinski, D. A.; Denes, P.; Joseph, J.; Lins, U.; Marchesini, S.; Shiu, H.-W.; Tyliszczak, T.; Shapiro, D. A. Measuring Spectroscopy and Magnetism of Extracted and Intracellular Magnetosomes using Soft X-ray Ptychography. *Proceedings of the National Academy of Sciences.* **2016,** *113* (51), E8219-E8227.

34. Shapiro, D. A.; Yu, Y.-S.; Tyliszczak, T.; Cabana, J.; Celestre, R.; Chao, W.; Kaznatcheev, K.; Kilcoyne, A. D.; Maia, F.; Marchesini, S. Chemical Composition

Mapping with Nanometre Resolution by Soft X-ray Microscopy. *Nature Photonics.* **2014,** *8* (10), 765-769.

35. Maiden, A.; Morrison, G.; Kaulich, B.; Gianoncelli, A.; Rodenburg, J. Soft X-ray Spectromicroscopy using Ptychography with Randomly Phased Illumination. *Nature Communications.* **2013,** *4* (1), 1-6.
36. Watts, B. Calculation of the Kramers-Kronig Transform of X-ray Spectra by A Piecewise Laurent Polynomial Method. *Optics Express.* **2014,** *22* (19), 23628-23639.
37. Dambach, S.; Backe, H.; Doerk, T.; Eftekhari, N.; Euteneuer, H.; Görgen, F.; Hagenbuck, F.; Kaiser, K.; Kettig, O.; Kube, G. Novel Interferometer in the Soft X-ray Region. *Physical Review Letters.* **1998,** *80* (25), 5473.
38. Jacobsen, C. *X-ray microscopy*. First Edition; Cambridge University Press: Cambridge, United Kingdom, **2019**.
39. Hornberger, B.; Feser, M.; Jacobsen, C. Quantitative Amplitude and Phase Contrast Imaging in a Scanning Transmission X-ray Microscope. *Ultramicroscopy.* **2007,** *107* (8), 644-655.
40. Obst, M., Fe 2p model spectra of iron oxides. Urquhart, S., Olumorin, T., Ed. *Private Communication,* **2019**.
41. US Research Nanomaterials Inc. Web Page. https://www.us-nano.com (accessed June 30, 2021).
42. Nanocomposix Web Page. https://nanocomposix.com (accessed June 30, 2021).
43. Fienup, J. R. Reconstruction of An Object From the Modulus of Its Fourier Transform. *Optics Letters.* **1978,** *3* (1), 27-29.
44. Sun, T.; Sun, G.; Yu, F.; Mao, Y.; Tai, R.; Zhang, X.; Shao, G.; Wang, Z.; Wang, J.; Zhou, J. Soft X-ray Ptychography Chemical Imaging of Degradation in A Composite Surface-Reconstructed Li-rich Cathode. *American Chemical Society Nano.* **2021,** *15* (1), 1475-85.
45. Hitchcock, A. P., Jacobsen, C., Zimba, C., et al. Axis2000 - Analysis of X-ray Images and Spectra. [Online]. http://unicorn.mcmaster.ca/axis/aXis2000-IDLVM.html (accessed March 8, 2021).
46. Yu, Y.-S.; Kim, C.; Shapiro, D. A.; Farmand, M.; Qian, D.; Tyliszczak, T.; Kilcoyne, A. D.; Celestre, R.; Marchesini, S.; Joseph, J. Dependence on Crystal Size of the Nanoscale

Chemical Phase Distribution and Fracture in Li_xFePO_4. *Nano Letters.* **2015,** *15* (7), 4282-4288.

47. Deng, J.; Nashed, Y. S. G.; Chen, S.; Phillips, N. W.; Peterka, T.; Ross, R.; Vogt, S.; Jacobsen, C.; Vine, D. J. Continuous Motion Scan Ptychography: Characterization for Increased Speed in Coherent X-ray Imaging. *Optics Express.* **2015,** *23* (5), 5438-5451.
48. Huang, X.; Lauer, K.; Clark, J. N.; Xu, W.; Nazaretski, E.; Harder, R.; Robinson, I. K.; Chu, Y. S. Fly-scan Ptychography. *Scientific Reports.* **2015,** *5* (1), 1-5.
49. Pelz, P. M.; Guizar-Sicairos, M.; Thibault, P.; Johnson, I.; Holler, M.; Menzel, A. On-The-Fly Scans for X-ray Ptychography. *Applied Physics Letters.* **2014,** *105* (25), 251101.
50. Clark, J. N.; Huang, X.; Harder, R. J.; Robinson, I. K. Continuous Scanning Mode For Ptychography. *Optics Letters.* **2014,** *39* (20), 6066-6069.
51. Zhou, S.-A.; Brahme, A., Development of Phase-contrast X-ray Imaging Techniques and Potential Medical Applications. *Physica Medica.* **2008,** *24* (3), 129-148.
52. Margaritondo, G. *Elements of Synchrotron Light: For Biology, Chemistry, and Medical Research*. Oxford University Press: New York, **2002**.
53. Pfeiffer, F.; Weitkamp, T.; Bunk, O.; David, C. Phase Retrieval and Differential Phase-contrast Imaging with Low-Brilliance X-ray Sources. *Nature Physics.* **2006,** *2* (4), 258-261.
54. Dierolf, M.; Menzel, A.; Thibault, P.; Schneider, P.; Kewish, C. M.; Wepf, R.; Bunk, O.; Pfeiffer, F. Ptychographic X-ray Computed Tomography at the Nanoscale. *Nature.* **2010,** *467* (7314), 436-439.
55. Odstrčil, M.; Holler, M.; Guizar-Sicairos, M. Arbitrary-Path Fly-Scan Ptychography. *Optics Express.* **2018,** *26* (10), 12585-12593.
56. Du, M.; Kandel, S.; Deng, J.; Huang, X.; Demortiere, A.; Nguyen, T. T.; Tucoulou, R.; De Andrade, V.; Jin, Q.; Jacobsen, C. Adorym: A Multi-Platform Generic X-ray Image Reconstruction Framework Based on Automatic Differentiation. *Optics Express.* **2021,** *29* (7), 10000-10035.
57. Gerchberg, R.; Saxton, W. Wave Phase From Image and Diffraction Plane Pictures. In *Image Processing and Computer-Aided Design in Electron Optics*. Academic Press: London and New York, **1973,** 66-81.

58. Elser, V. Phase Retrieval By Iterated Projections. *Journal of the Optical Society of America A.* **2003,** *20* (1), 40-55.

59. Guizar-Sicairos, M.; Diaz, A.; Holler, M.; Lucas, M. S.; Menzel, A.; Wepf, R. A.; Bunk, O. Phase Tomography From X-ray Coherent Diffractive Imaging Projections. *Optics Express.* **2011,** *19* (22), 21345-21357.

60. Hirose, M.; Ishiguro, N.; Shimomura, K.; Nguyen, D.-N.; Matsui, H.; Dam, H. C.; Tada, M.; Takahashi, Y., Oxygen-Diffusion-Driven Oxidation Behavior and Tracking Areas Visualized by X-ray Spectro-ptychography with Unsupervised Learning. *Communications Chemistry.* **2019,** *2* (1), 1-7.

61. Yuan, H.; Yuan, H.; Casagrande, T.; Shapiro, D.; Yu, Y.-S.; Enders, B.; Lee, J. R.; van Buuren, A.; Biener, M. M.; Gammon, S. A. 4D Imaging of ZnO-Coated Nanoporous Al_2O_3 Aerogels by Chemically Sensitive Ptychographic Tomography: Implications For Designer Catalysts. *American Chemical Society Applied Nano Materials.* **2021,** *4* (1), 621-632.

62. Yusuf, M.; Zhang, F.; Chen, B.; Bhartiya, A.; Cunnea, K.; Wagner, U.; Cacho-Nerin, F.; Schwenke, J.; Robinson, I. Procedures For Cryogenic X-ray Ptychographic Imaging of Biological Samples. *International Union of Crystallography Journal.* **2017,** *4* (2), 147-151.

63. Thibault, P.; Menzel, A., Reconstructing State Mixtures From Diffraction Measurements. *Nature.* **2013,** *494* (7435), 68-71.

64. Kewish, C. M.; Thibault, P.; Dierolf, M.; Bunk, O.; Menzel, A.; Vila-Comamala, J.; Jefimovs, K.; Pfeiffer, F. Ptychographic Characterization of the Wavefield in The Focus of Reflective Hard X-ray Optics. *Ultramicroscopy.* **2010,** *110* (4), 325-329.

65. Björling, A.; Kalbfleisch, S.; Kahnt, M.; Sala, S.; Parfeniukas, K.; Vogt, U.; Carbone, D.; Johansson, U. Ptychographic Characterization of A Coherent Nanofocused X-ray Beam. *Optics Express.* **2020,** *28* (4), 5069-5076.

66. Karunakaran, C., Wang, J., Lu, Y., Dynes, J., Hitchcock, A., and Urquhart, S. Canadian Light Source Soft X-ray Microscopy (SM) Beamline Manual Scanning Transmission X-ray Microscopy (STXM) Branch. [Online]. https://sm.lightsource.ca/media/uploads/110613_sm_beamlinemanual-jjd.pdf (accessed March 8, 2021).